

Vulnerability of fault-tolerant topological quantum error correction to quantum deviations in code space

Yuanchen Zhao^{1,2} and Dong E. Liu^{1,2,3,4,*}

¹State Key Laboratory of Low Dimensional Quantum Physics,
Department of Physics, Tsinghua University, Beijing, 100084, China

²Frontier Science Center for Quantum Information, Beijing 100184, China

³Beijing Academy of Quantum Information Sciences, Beijing 100193, China

⁴Hefei National Laboratory, Hefei 230088, China

(Dated: March 11, 2025)

Quantum computers face significant challenges from quantum deviations or coherent noise, particularly during gate operations, which pose a complex threat to the efficacy of quantum error correction (QEC) protocols. In this study, we scrutinize the performance of the topological toric code in 2 dimension (2D) under the dual influence of stochastic noise and quantum deviations, especially during the critical phases of initial state preparation and error detection facilitated by multi-qubit entanglement gates. By mapping the protocol for multi-round error detection—from the inception of an imperfectly prepared code state via imperfect stabilizer measurements—to a statistical mechanical model characterized by a 3-dimensional \mathbb{Z}_2 gauge theory coupled with a 2-dimensional \mathbb{Z}_2 gauge theory, we establish a novel link between the error threshold and the model's phase transition point. Specifically, we find two distinct error thresholds that demarcate varying efficacies in error correction. The empirical threshold that signifies the operational success of QEC aligns with the theoretical ideal of flawless state preparation operations. Contrarily, below another finite theoretical threshold, a phenomenon absent in purely stochastic error models emerges: unidentifiable measurement errors precipitate QEC failure in scenarios with large code distances. For codes of finite or modest distance d , it is revealed that maintaining the preparation error rate beneath a crossover scale, proportional to $1/\log d$, allows for the suppression of logical errors. Considering that fault-tolerant quantum computation is valuable only in systems with large scale and exceptionally low logical error rates, this investigation explicitly demonstrates the serious vulnerability of fault tolerant QEC based on 2D toric codes to quantum deviations in code space, highlighting the imperative to address inherent preparation noise.

I. Introduction

Quantum supremacy was recently observed in quantum processors [1–3], which is a milestone in the field of quantum computation. However, the state-of-the-art quantum devices [1–8] are classified as noisy intermediate-scale quantum (NISQ) [9] computer, and the observed quantum supremacy is only a weakened version with few practical applications [9]. To date, the merely known examples with worthwhile quantum advantages are only expected in fault tolerant quantum computers with quantum error correction (QEC) [10–12]. Recently, QEC codes with small size have recently been tested in experiments [6, 13–25].

A cornerstone of fault tolerance is the "error threshold theorem." It posits that if the physical error rates across all facets of quantum computation—including code state preparation, stabilizer checks, logical operations, and readout—remain beneath a finite threshold, then one can achieve arbitrary logical accuracy within a noisy quantum device [26–28]. The threshold theorem is well-established if the device noise can be captured by independent stochastic errors [26, 28–34], including circuit-level noise models [35, 36]. However, actual quantum devices suffer from more general type of errors. With correlated errors, the threshold theorem is modified for a more conceptual infidelity measure, e.g. diamond norm [27], for correlations with weak amplitude [37] and

short length [38], and for the environment with critical behaviors [39, 40]. A more practical type of noise comes from imperfect calibration and control of gate operations, causing quantum deviation or coherent effect in errors. This problem motivated recent studies of the independent single-qubit coherent errors [41–49] and the detection induced coherent errors from entanglement gate noise [50–52]. We emphasize that the two-qubit entanglement gates are much harder to calibrate and more error-prone than single-qubit gates. Comprehending the fault-tolerance and error threshold theorem in practical quantum systems exhibiting coherent deviations proves to be formidable, primarily due to the scarcity of analytical and numerical methodologies. Although an efficient numerical strategy exists for a special case [43], the general coherent error problems, that go beyond the Clifford algebra, cannot be simulated efficiently in classical computers. Additionally, previous studies on QEC error thresholds have seldom addressed quantum deviations in code state preparation and error detection. This motivates us to develop a theoretical framework to study the elusive and unavoidable quantum deviations alone with stochastic errors in realistic QEC procedures and establish a more practical error threshold theorem.

Summary of main results: In this work, we study the robustness of the toric code QEC [53], under the influence of imperfect state preparation and measurements, as visualized in Fig. 1, along with stochastic Pauli errors afflicting physical qubits. We consider the realistic case that the measurement apparatus, crucial for both the preparation of the initial state and the subsequent error detection steps, is com-

* Corresponding to: dongeliu@mail.tsinghua.edu.cn

promised by coherent noise. The initialization of code states is facilitated through an initial round of stabilizer measurements, following which these states are subjected to an error correction regimen, where the common multi-round syndrome measurements method [29, 30] is used to decode errors. Such a procedure is also adopted by experiments [24].

Further, we transition the operational framework of this QEC protocol into a novel statistical mechanical (SM) model, characterized by the integration of a 3-dimensional \mathbb{Z}_2 gauge theory with a 2-dimensional \mathbb{Z}_2 gauge theory. This integration is achieved via a distinctive, non-local time-like coupling originates from the imperfection during initial state preparation. This conceptual model serves as the basis for our exploration into the interaction dynamics between quantum error correction processes and the pervasive influences of coherent noise and stochastic errors, thereby offering novel insights into the resilience and limitations of the toric code QEC methodology under practical conditions. We also emphasize the theoretical novelty in deriving an explicit SM model with coherent errors, as typically, such models are limited to stochastic Pauli errors and Clifford structures.

We find that the Wilson loops in this SM model have an anisotropic behavior: The timelike Wilson loops deconfine at low temperatures (small physical error rates) and confine at high temperatures (large physical error rates); but the spacelike Wilson loops confine at any finite temperature, resulting from the non-local timelike correlation. Then, we predict that there are two thresholds in our QEC model. The confinement-deconfinement transition point of timelike Wilson loops signifies a theoretical threshold located at finite measurement error rate and finite Pauli error rate. However, the confinement behavior of spacelike Wilson loops suggests that the practical measurement error threshold seats at the point where the initial state preparation is perfect. With arbitrary finite preparation error, the measurement errors will no longer be distinguished from Pauli errors, which results in the failure of QEC even in the limit of large code distance. With a finite code distance d , the effectiveness of the pragmatic QEC approach remains viable when the error rate associated with state preparation falls within a region $\sim 1/\log d$. Finally, we emphasize that a more realistic imperfect measurement model relating to Fig. 1(b) will in general has a worse performance.

II. Model for toric code under imperfect measurement

We follow the construction of topological surface code on a torus, i.e. toric code [29, 30, 33, 53]. There are two kinds of stabilizers associated with vertices and plaquettes respectively as shown in Fig. 1(a),

$$A_{v_0} = \prod_{e_0|v_0 \in \partial e_0} X_{e_0}, \quad B_{p_0} = \prod_{e_0 \in \partial p_0} Z_{e_0}. \quad (1)$$

Here we use the symbols v_0 and p_0 to label vertex and plaquette operators. X_{e_0} and Z_{e_0} represent Pauli operators acting on qubit e_0 (i.e. ‘‘edge’’). We assume the lattice contains N vertices, N plaquettes and $2N$ edges. $2N$ physical qubits

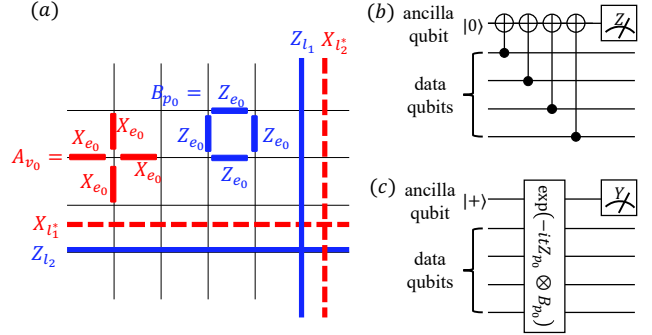


FIG. 1. (a) Toric code defined on 2D periodic lattice. Physical qubits stay on the edges of the lattice. The two kinds of stabilizers are $A_{v_0} = \prod_{e_0|v_0 \in \partial e_0} X_{e_0}$ defined on each vertex and $B_{p_0} = \prod_{e_0 \in \partial p_0} Z_{e_0}$ defined on each plaquette as shown in the figure. l_1 and l_2 denote non-contractible loops on the periodic lattice. The logical Pauli Z operators Z_{l_1} and Z_{l_2} are product of Z 's along these non-contractible loops. Correspondingly the logical Pauli X operators $X_{l_1}^*$ and $X_{l_2}^*$ are defined as X 's along non-contractible loops on the dual lattice l_1^* and l_2^* . They satisfy the commutation relations $X_{l_1}^* Z_{l_1} = -Z_{l_1} X_{l_1}^*$, $X_{l_2}^* Z_{l_2} = -Z_{l_2} X_{l_2}^*$, $X_{l_1}^* Z_{l_2} = Z_{l_2} X_{l_1}^*$, $X_{l_2}^* Z_{l_1} = Z_{l_1} X_{l_2}^*$ and acts respectively on two different logical qubits of toric code. (b) A realistic circuit for B_{p_0} measurement [30]. The ancilla qubit is prepared in $|0\rangle$ state, then four $CNOT$ gates are applied in order to couple data and ancilla qubits. Finally, the ancilla is projectively measured in Z basis. (c) A simplified B_{p_0} measurement circuit considered in our work. Note that a five-qubit unitary gate is used here instead of four two-qubit gates. To enable a theoretical analysis of the problem, we focus on the case (c) in our model: (1) Prepare the ancilla qubit in $|+\rangle$ state for each plaquette p_0 ; (2) apply a joint time evolution involving each ancilla and its four neighboring data qubits $\exp[-itZ_{p_0} \otimes B_{p_0}]$ where Z_{p_0} is the Pauli Z acting on ancilla at p_0 ; (3) perform projective measurement on ancilla in Y basis. This model is a rather simplified one which is easier to study analytically, but it can capture the fundamental influence of imperfect stabilizer measurement on QEC. A more realistic imperfect measurement model relating to (b) will in general has a worse performance, see the discussion of Eq. (24). A similar construction can also be applied to A_v stabilizers.

are put on each edge of the lattice. Its four-dimensional code subspace is stabilized by all A_{v_0} 's and B_{p_0} 's which is achieved through projective measurement of these stabilizers. Specifically, we start with the logical $++$ state by projecting all the B_{p_0} 's to $+1$ for a product state of physical qubits $\bigotimes_{e_0} |+\rangle_{e_0}$:

$$|++\rangle = \prod_{p_0} \frac{I + B_{p_0}}{2} \bigotimes_{e_0} |+\rangle_{e_0} \quad (2)$$

and other three logical bases are obtained by applying logical Pauli Z operators $\{Z_{l_1}, Z_{l_2}\}$ as shown in Fig. 1(a), and these four logical bases form a code subspace \mathcal{C} . Correspondingly there are also logical Pauli X operators $\{X_{l_1}^*, X_{l_2}^*\}$.

Experimentally, the stabilizer measurements are implemented using a multi-qubit unitary operation on a combined qubit set consisting of four data qubits and an ancilla qubit, followed by an ancilla qubit measurement [30, 54], also refer

to Fig.1(b). The correct projective measurements of stabilizers can only be achieved through ideal unitary operations. However, the multi-qubit operation in principle cannot avoid the miscalibration in the experimental setups and results in imperfect measurement [51]. Here we consider a simplified imperfect measurement model [52] with a joint time evolution involving each ancilla and its four neighboring data qubits $\exp[-itZ_{p_0} \otimes B_{p_0}]$ [refer to Fig.1(c)]. Then equivalently we get an operator acting on the data qubits

$$M_{\{s_{p_0}\}} = \frac{1}{(\sqrt{2} \cosh \beta)^N} \exp \left[\frac{1}{2} \beta \sum_{p_0} s_{p_0} B_{p_0} \right]. \quad (3)$$

up to an irrelevant global phase factor. Note that $M_{\{s_{p_0}\}}$ is not a unitary operator. Here $\tanh(\beta/2) = \tan t$, and $s_{p_0} = \pm 1$ is the measurement outcome of ancilla qubit at p_0 . We use $\{s_{p_0}\}$ to denote the configuration of ancilla measurement outcomes, which appears with probability $\text{tr}(M_{\{s_{p_0}\}} \rho M_{\{s_{p_0}\}}^\dagger)$ for a given initial state ρ of data qubits.

It is easy to verify that the $E_{\{s_{p_0}\}} = M_{\{s_{p_0}\}}^\dagger M_{\{s_{p_0}\}}$ operators form a set of positive operator-valued measurement (POVM). The error model [52] only considers the miscalibration of the evolution time t with $0 \leq t \leq \pi/4$. When $t = \pi/4$, we have $\beta \rightarrow +\infty$ in Eq. (3) and recover the correct projective measurement $M_{\{s_{p_0}\}} \propto \prod_{p_0} (I + s_{p_0} B_{p_0})/2$. For $t < \pi/4$ the parameter β is finite, and $M_{\{s_{p_0}\}}$ will no longer be a stabilizer projection. Here we will assume the coherent deviation $\delta t = t - \pi/4 > 0$ to be a fixed value, while in Sec.SVI of supplemental information (SI) [55], we briefly discuss the case when it is randomly distributed. Generally, β measures how close is our imperfect measurement to the ideal projective measurement.

Experimentally while preparing the initial logical state through stabilizer measurement as in Eq. (2), the coherent noises are unavoidable, especially for the entanglement gates. For the imperfect measurement model we adopt (Eq. (3)), the imperfect initial logical $++$ state is considered as

$$|\widetilde{++}\rangle = \frac{M_{\{+\}} \otimes_{e_0} |+\rangle_{e_0}}{\sqrt{\otimes_{e_0} \langle +|_{e_0} M_{\{+\}}^\dagger M_{\{+\}} \otimes_{e_0} |+\rangle_{e_0}}}, \quad (4)$$

where all the ancilla measurement outcomes s_{p_0} are set to +1. We define the other three logical states by applying logical Z operators in analogy to experimental setups, $|\widetilde{-+}\rangle = Z_{l_1} |\widetilde{++}\rangle$, $|\widetilde{+-}\rangle = Z_{l_2} |\widetilde{++}\rangle$ and $|\widetilde{--}\rangle = Z_{l_1} Z_{l_2} |\widetilde{++}\rangle$. Note that those states are still orthogonal to each other, and define the corresponding code space $\widetilde{\mathcal{C}}(\beta)$ as the subspace spanned by the above four states (refer to Sec.SI of SI [55] for more details). Unlike the perfect measurement case, those logical states depend on the choice of logical operators about where they are located on the physical lattice. However, the key results presented in this work—the statistical mechanical model and its implications to QEC—remain unaffected by the particular selection of logical operators.

These states are argued to be non-topological [52, 56] by a mapping to the two-dimensional (2D) \mathbb{Z}_2 lattice gauge theory. Such states may challenge QEC, yet the behavior

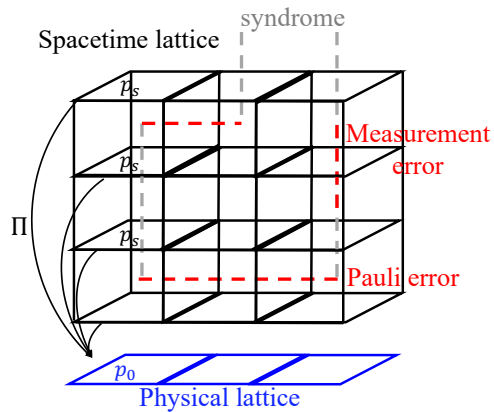


FIG. 2. 3D spacetime of error history. The black lattice is the spacetime lattice. At the spatial direction, we take periodic boundary condition; at the temporal direction, we assume that the QEC starts at $t = -\infty$ and ends at $t = +\infty$, such that the 3D corresponding spacetime lattice has infinite boundary condition at time direction. These boundary conditions are also adopted in Ref. [29] when discussing SM mapping. The Pauli errors, measurement errors and error syndromes are represented as strings on the dual lattice (dashed lines that cross plaquettes). We use timelike and spacelike dual strings to represent measurement errors, i.e. faulty syndromes caused by imperfection of sequential measurements, and Pauli errors, respectively. Given a configuration of Pauli X error (horizontal red strings) for the entire history, the error syndrome (vertical gray strings) will be the configuration of -1 ancilla measurement outcomes at different time steps. The error syndrome is supposed to match the endpoints of Pauli error strings, but due to imperfection of syndrome measurements, the syndrome outcomes might be flipped with certain probability. Those flipped syndromes will be referred to as measurement errors (vertical red strings). Π denotes the projection from the 3D spacetime lattice to the 2D physical lattice. Given a plaquette p_s , $\Pi(p_s)$ yields a plaquette p_0 at the same spatial location as p_s .

of practical QEC procedures and the corresponding error thresholds remains an open question. Indeed, Ref. [57] suggests that in the presence of stochastic noise, the mixed-state topological phase transition happens before the recoverability transition, given that topological properties are defined by local operations and recovery can involve non-local operations. Additionally, for general imperfect initial codes considered as approximate QEC, Ref. [58] identifies non-topological states that correct certain local errors in large systems. Consequently, it is essential to assess a specific QEC protocol with imperfect measurements and directly analyze its error threshold characteristics.

III. Statistical mechanical mapping

Normally for toric code, the Pauli errors are detected by syndrome measurement. However, the syndrome measurement also suffers from imperfection resulting in faulty outcomes. Therefore, in order to distinguish measurement errors from Pauli errors, the standard procedure is to perform

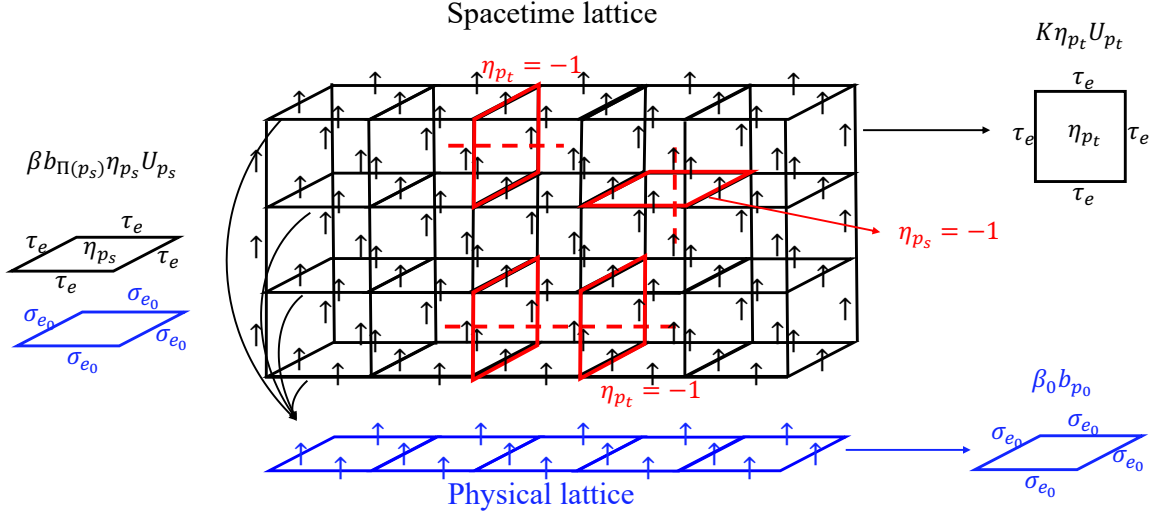


FIG. 3. Illustration of the SM model we obtained in Eq. (10). The τ_e spins are defined on the edges of 3D spacetime lattice and the σ_{e_0} spins lie on 2D physical lattice. There are three types of interactions in this model as shown in this figure. $\beta_0 b_{p_0}$ is the gauge interaction term defined on the physical lattice. $K \eta_{p_t} U_{p_t}$ is the timelike gauge interaction on spacetime lattice. The $\beta b_{\Pi(p_s)} \eta_{p_s} U_{p_s}$ term couples the spacelike gauge interaction term U_{p_s} to the gauge interaction term $b_{\Pi(p_s)}$ on physical lattice. The η_p 's set the signs of gauge interactions on spacetime lattice and they mark the position of error strings during the QEC procedure in Fig. 2. For example, the flipped interaction $\eta_p = -1$ at plaquette p (red plaquette) corresponds to the presence of an error string at p (dashed red line). The $\{\eta_p\}$ configuration follows a disorder probability Eq. (5) that comes from the randomness of Pauli errors and in syndrome measurement. The τ_e spins are non-locally correlated at timelike direction since all spacelike plaquette interactions U_{p_s} along the same timelike arrow are all coupled to the same $b_{\Pi(p_s)}$. Meanwhile, the disorder probability Eq. (5) is also correlated at time direction. Physically this is due to the fact imperfection measurement operator will change the current quantum state, which in turn affects subsequent measurement results. It is evident from the expressions Eq. (10) and Eq. (5) that the non-local correlation results from finite β_0 , or in other words imperfect initial state preparation.

multi rounds of syndrome measurements and take into account the obtained entire error history while decoding [29]. Note that Ref. [29] only consider the stochastic errors of the ancilla measurement and assume a well-prepared initial state from the perfect code space, but we consider imperfect entanglement operations which affect both the initial state preparation and the error detection. We model the QEC procedure as follows (for convenience we consider only the sector from Pauli X errors):

- (1) Start with an arbitrary state $|\tilde{\Psi}\rangle \in \tilde{\mathcal{C}}(\beta_0)$, the imperfect measurement strength while preparing the initial state is β_0 .
- (2) Probabilistic Pauli X error acts at each integer valued time $t = -\infty, \dots, -1, 0, 1, \dots, +\infty$. The X error at each physical qubit on each time slice occurs independently with probability $q \in [0, 1/2]$.
- (3) Perform a round of syndrome measurement for each time interval between t and $t + 1$. The syndrome measurements are assumed to still suffer from imperfect measurement. So given a configuration of syndrome measurement outcomes $\{s_{p_0}\}$ for a single round, it leads to the action of $M_{\{s_{p_0}\}}$ operator on the current quantum state. Here we set the strength of syndrome measurements to be β in order to distinguish them from initial state preparation.

- (4) At the end of the QEC procedure, we decode and apply the Pauli X correction operator to the final state.

We first notice that our model ensures that the imperfection of measurement exclusively affects stabilizer bits while leaving logical information undisturbed, since $M_{\{s_{p_0}\}}$ commutes with logical operators. So, if the Pauli X errors and the final correction operator compose a contractible loop, we can verify that the logical information will still be preserved. We refer to this case as the success of QEC, in contrast to the situation with a non-contractible loop causing a logical error. Note that this condition for successful QEC is the same as the one in Ref. [29].

The above QEC procedure could be diagrammatically represented on a three dimensional (3D) cubic lattice in order to decode as in Fig. 2. The error strings (including both measurement and Pauli parts) and syndrome strings (marked with -1 ancilla outcomes) together compose closed strings or with only endpoints at infinity. The task of the decoder is to identify both measurement and Pauli errors. In order to do so, the decoder should select a configuration of strings (decoding strings) connecting the endpoints of syndrome strings. The timelike (spacelike) parts of the decoding strings represent the measurement (Pauli) error identified by the decoder. QEC succeeds if and only if the decoding strings are topologically equivalent to the real error strings (form contractible loops). So given an error syndrome, the optimal decoder algorithm [38] should select the topological equivalent class of error strings with the largest probability.

Our main result is that we mapped this QEC scenario to an statistical mechanical (SM) model. We denote the vertex, edge and plaquette of the 3D spacetime lattice as v , e and p . Specifically, the spacelike (timelike) edges and plaquettes will be labeled with a subscript s (t), such as e_s and p_s (e_t and p_t). We assign a variable $\eta_p = \pm 1$ to each plaquette p to represent the error configuration, e.g. $\eta_p = -1$ for where the measurement or Pauli error presents and $+1$ otherwise. Then the probability of a given error configuration $\{\eta_p\}$ will be

$$P(\{\eta_p\}) = \frac{\sum_{\{\sigma_{e_0}\}} \exp \left[\beta_0 \sum_{p_0} b_{p_0} + \beta \sum_{p_s} b_{\Pi(p_s)} \eta_{p_s} + K \sum_{p_t} \eta_{p_t} \right]}{4^N (\cosh^N \beta_0 + \sinh^N \beta_0) (2 \cosh \beta)^{NT} (2 \cosh K)^{2NT}}, \quad (5)$$

where

$$b_{p_0} = \prod_{e_0 \in \partial p_0} \sigma_{e_0}, \quad K = -\frac{1}{2} \log \frac{q}{1-q}. \quad (6)$$

Here σ_{e_0} is a classical \mathbb{Z}_2 spin-like variable assigned to each edge e_0 of the 2D physical lattice. b_{p_0} is the product of four neighbouring σ_{e_0} 's around the plaquette p_0 , which has the similar form to a \mathbb{Z}_2 gauge interaction term [59, 60]. $\Pi(p_s)$ is the projection of the spacelike plaquette p_s onto the 2D physical lattice, as in Fig. 2. The label T represents the total number of time steps, and will eventually be taken to $+\infty$. The summation $\sum_{\{\sigma_{e_0}\}}$ runs over all $\{\sigma_{e_0}\}$ configurations.

The detailed derivation of Eq. (5) can be found in Sec. SI of SI [55], and we only list some key steps here. Notice that given a quantum state ρ , the probability of POVM outcome is $\text{tr}(E_{\{s_{p_0}\}} \rho)$. We may construct a probability of syndrome measurement outcomes of all time steps and space locations conditioned on a fixed Pauli error configuration, which is expressed as

$$P(\{s_{p_0}(t)\}_t | \{\eta_{e_0}(t)\}_t) = \left\| \prod_t M_{\{s_{p_0}(t)\}} X_{\{\eta_{e_0}(t)\}} |\tilde{\Psi}\rangle \right\|^2 \quad (7)$$

for an arbitrary initial state $|\tilde{\Psi}\rangle$ in the imperfect code space $\tilde{\mathcal{C}}(\beta_0)$. Specifically, any initial state should be a superposition of imperfect logical states $|\tilde{\Psi}\rangle = \Psi_{++} |++\rangle + \Psi_{+-} |+-\rangle + \Psi_{-+} |-+\rangle + \Psi_{--} |--\rangle$ and we assume it to be normalized. Here we introduced the label t to specify the time step. $\{s_{p_0}(t)\}$ and $\{\eta_{e_0}(t)\}$ denote the syndrome configuration and Pauli error configuration at time t , while $\{s_{p_0}(t)\}_t$ and $\{\eta_{e_0}(t)\}_t$ denote the configurations of the whole history. Note that a pair (p_0, t) yields a corresponding spacelike plaquette p_s and a pair (e_0, t) yields a corresponding timelike plaquette p_t . $X_{\{\eta_{e_0}(t)\}}$ is the total Pauli error operator at time t , and has the form

$$X_{\{\eta_{e_0}(t)\}} = \prod_{e_0} (\delta_{\eta_{e_0}(t), +1} I + \delta_{\eta_{e_0}(t), -1} X_{e_0}). \quad (8)$$

After combining with Pauli error probability

$$P(\{\eta_{e_0}(t)\}_t) = \prod_{e_0, t} q^{\delta_{\eta_{e_0}(t), -1}} (1-q)^{\delta_{\eta_{e_0}(t), +1}} = \prod_{e_0, t} \frac{\exp(K \eta_{e_0}(t))}{2 \cosh K}, \quad (9)$$

we can obtain the joint probability of total error configurations $P(\{\eta_{p_0}(t)\}_t, \{\eta_{e_0}(t)\}_t)$, which is exactly Eq. (5) after converting the notations to those of the 3D lattice (we now denote $\{\eta_p\} = \{\eta_{p_0}(t), \eta_{e_0}(t)\}_t$).

Then following the standard procedure described in Ref. [29, 33, 38], we computed the probability of the topological equivalent class of error configurations. by introducing the gauge interaction term U_p , the summation over topologically equivalent error configurations is converted to the summation of spin configurations $\{\tau_e\}$ up to a constant factor. The result is proportional to the partition function of an SM model

$$P(\{\{\eta_p\}\}) \propto \mathcal{Z}(\{\eta_p\}) = \sum_{\{\sigma_{e_0}, \{\tau_e\}\}} \exp \left[\beta_0 \sum_{p_0} b_{p_0} + \beta \sum_{p_s} b_{\Pi(p_s)} \eta_{p_s} U_{p_s} + K \sum_{p_t} \eta_{p_t} U_{p_t} \right], \quad U_p = \prod_{e \in \partial p} \tau_e. \quad (10)$$

This SM model is a 3D \mathbb{Z}_2 gauge theory defined on the spacetime lattice coupled to a 2D \mathbb{Z}_2 gauge theory defined on the physical lattice, see Fig. 3. Here $\tau_e = \pm 1$ is a spin variable defined on each edge e of the spacetime lattice. U_p is an ordinary \mathbb{Z}_2 gauge interaction term containing four τ_e operators, $\{\{\eta_p\}\}$ denotes the topological equivalent class represented by $\{\eta_p\}$, and η_p sets the sign of interaction term on each plaquette. Physically, those τ_e operators describe the fluctuation of error strings, since flipping τ_e operator is equivalent to deforming the error strings represented by $\{\eta_p\}$. Therefore, the model acquires a local symmetry

$$\eta_p \rightarrow \eta_p \prod_{e \in \partial p} \nu_e, \quad \tau_e \rightarrow \tau_e \nu_e, \quad \nu_e = \pm 1, \quad (11)$$

which ensures that topologically equivalent error configurations yield the same partition function.

In order to detect the error threshold, Eq. (5) can be considered as the quenched disorder probability of interaction configuration $\{\eta_p\}$. Then the phase transition point of τ_e spins in the disordered SM model corresponds to the error threshold of the QEC model [29, 33, 38]. Note that the 2D gauge model, derived from initial state imperfections [52, 56], and the 3D gauge model, characterizing error string fluctuations [29], couple to form a novel system illuminating imperfect initial states' effects on QEC.

IV. Phase structure of the statistical mechanical model

First, we notice that the SM model has a non-local correlation at time direction originates from imperfect initial state preparation, see Fig. 3. If the initial state is well prepared

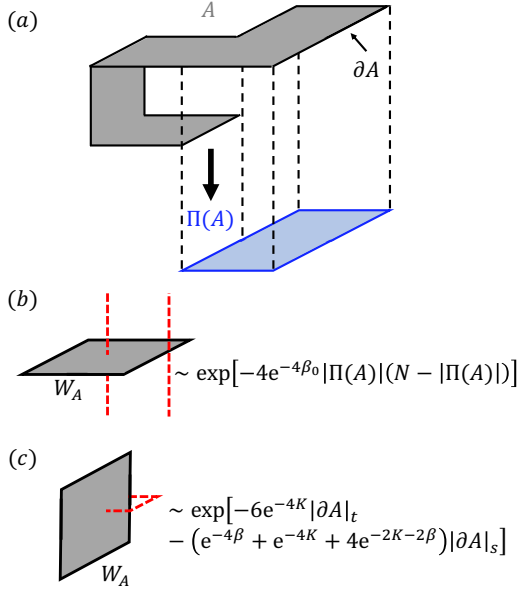


FIG. 4. (a) Example of a Wilson loop. A is a surface in 3D spacetime (gray) and ∂A is its boundary (black), which is a closed loop. $\Pi(A)$ is the projection of surface A from 3D spacetime to 2D space mod \mathbb{Z}_2 . Specifically, under projection the timelike plaquettes are dropped, and an even number of spacelike plaquettes at the same space position also vanishes. The only remaining plaquettes are at the spatial locations that originally have odd numbers of spacelike plaquettes. In (b) and (c), the black lines represent Wilson loops and the red dashed lines are examples of topologically trivial error strings created by τ_e fluctuation. (b) A spacelike Wilson loop. In a large enough system it decays exponentially with respect to the area for any finite temperature. For a large region A , the areal decay will be much faster than the perimetric decay, so the first term in Eq. (16) dominates. This behavior is contributed by the fluctuation of infinite long timelike error strings which are able to appear at any space position (see Sec.IV of SI [55]). (c) A timelike Wilson loop. Under a low temperature, it decays exponentially with respect to the perimeter. Note that both timelike edges and spacelike edges are contained in the boundary of a timelike region, determining the $|\partial A|_t$ term and $|\partial A|_s$ term respectively.

($\beta_0 \rightarrow \infty$), the code space $\tilde{\mathcal{C}}(\beta_0)$ becomes exactly the toric code subspace. The action of following syndrome measurement operators Eq. (3) on this space yields only a global phase factor and does not change the state itself. In this case, the model reduces to the familiar random plaquette gauge model (RPGM) [29, 61, 62].

In reality, the faulty circuits that produce the imperfect syndrome measurements also provide the imperfect initial state preparations. In this situation, i.e. with finite β_0 , the non-local timelike correlation will lead to a different phase structure in stark contrast to RPGM. In order to detect the phase diagram of this model, we consider the Wilson loop

$$W_A = \prod_{p \in A} U_p = \prod_{e \in \partial A} \tau_e, \quad (12)$$

which serves as the order parameter for \mathbb{Z}_2 gauge theory.

Here A is a set of plaquettes representing a surface in spacetime. The product of U_p 's on surface A equals the product of τ_e 's on ∂A , which is the boundary of surface A and forms a closed loop. In the conventional \mathbb{Z}_2 gauge theory [59, 60] the scaling behavior of Wilson loop expectation values with respect to the loop size distinguishes between the confinement (disordered) phase and the deconfinement (ordered) phase. In the deconfinement phase, it decays exponentially with respect to the perimeter of the loop,

$$W_A \sim \exp(-const \times |\partial A|), \quad (13)$$

called perimeter law. Here we use $|\cdot|$ to denote the cardinal of a set (i.e. the number of the elements of a set). For example $|\partial A|$ is the number of edges contained in ∂A . On the other hand, in the confinement phase, the scaling behavior of Wilson loops obeys area law,

$$W_A \sim \exp(-const \times |A_{min}|), \quad (14)$$

where A_{min} is the minimal surface enclosed by ∂A . Here we will study the expectation value of Wilson loops in our SM model.

Note that our SM model satisfies a generalized version of Nishimori condition [63], which means that the error rate parameters (β_0, β, K) in the quenched disorder probability in Eq. (5) are the same as those in the partition function in Eq. (10), respectively. Under this condition, by taking advantage of a local symmetry of the model shown in Eq. (11), we find that (refer to Sec.III of SI [55])

$$[\langle W_A \rangle] = [\langle W_A \rangle^2]. \quad (15)$$

The above equality suggests the absence of gauge glass phase [61], where $[\langle W_A \rangle]$ obeys area law Eq. (14) but $[\langle W_A \rangle^2]$ obeys perimeter law Eq. (13). In that case, we only need to concern about the deconfinement-confinement phase transition of τ_e 's under Nishimori condition.

We then perform a low-temperature (i.e. β_0, β and K are sufficiently large, corresponding to small enough physical error rates) expansion [60] for $[\langle W_A \rangle]$. Here, $\langle \cdot \rangle$ denotes the ensemble average with respect to the model Eq.(10) under a specific configuration; and $[\cdot] = \sum_{\{\eta_p\}} P(\{\eta_p\}) \langle \cdot \rangle$ represents the disorder average over different configurations with respect to the probability Eq.(5). We assume $e^{-\beta_0}$, $e^{-\beta}$ and e^{-K} are of the same order and expand $\log[\langle W_A \rangle]$ up to the first non-vanishing order $e^{-4\beta_0}$. We obtain the result

$$[\langle W_A \rangle] \simeq \exp[-4e^{-4\beta_0}|\Pi(A)|(N - |\Pi(A)|) - (e^{-4\beta} + e^{-4K} + 4e^{-2\beta-2K})|\partial A|_s - 6e^{-4K}|\partial A|_t]. \quad (16)$$

Here Π is defined as projection from 3D spacetime to 2D space mod \mathbb{Z}_2 , illustrated in Fig. 4(a). $|\partial A|_s$ ($|\partial A|_t$) denotes the spacelike (timelike) edges e_s (e_t) contained in ∂A . The derivation of the expansion is lengthy and refer to Sec.IV of SI [55] for details.

Eq. (16) provides us with insights into the phase structure. As we have mentioned, the Wilson loops have anisotropic scaling behavior at low temperatures. A pure timelike Wilson loop W_A which contains only timelike plaquettes is

shown in Fig. 4(c). It deconfines and decays exponentially with respect to perimeter as in a conventional 3D \mathbb{Z}_2 lattice gauge theory under low temperature. Meanwhile, a pure spacelike Wilson loop is shown in Fig. 4(b). For large enough system size N , its areal decay is faster than the perimeteric decay, so the first term in Eq. (16) dominates and $[\langle W_A \rangle]$ confines as long as the temperature is finite. We notice that no matter how low the non-zero temperature is, the confinement is always maintained. In addition, a sufficiently high temperature should always drive the system into a completely disordered phase, which will confine all Wilson loops. Thus the spacelike Wilson loops confine at any finite temperature (or error rate). In comparison, if the initial state is ideally prepared ($\beta_0 = +\infty$, corresponds to RPGM), the Wilson loops will acquire an isotropic scaling behavior, i.e. both the spacelike and timelike Wilson loops will exhibit perimeteric decay at the low-temperature phase and areal decay at the high-temperature phase [29]. The qualitative phase diagram is summarised in Fig. 5 (a).

V. Impact on quantum error correction

Following the mapping of our QEC model to an SM model, we now examine its implications on QEC performance and the threshold theorem.

A. Behavior in an infinite size system

First of all, recognizing the existence of a confinement transition point concerning timelike Wilson loops in the limit $T \rightarrow +\infty$ and $N \rightarrow +\infty$, we ascertain that it also separates different behaviors of logical error rate. In fact, we find that the logical errors associated with spacelike non-contractible loops are suppressed at the low-temperature phase, indicating a transition we refer to as the theoretical threshold. In our derivation of low-temperature expansion (Sec.SIV of SI [55]), we find that:

1. The decay in area law for spacelike Wilson loops is attributed to the emergence of non-local timelike error strings as depicted in Fig. 4(b);
2. At sufficiently low temperatures, non-local timelike strings and local error loops manifest with relative independence, resulting in the confinement of local error loops, thereby preventing their extension to arbitrary lengths.

Specifically, this implies that fluctuating error strings are constrained (or unable to extend indefinitely) in their spatial extension, leading to a negligible error rate for spacelike non-contractible loops or logical Pauli operators. By examining the domain wall free energy cost [29] associated with these non-contractible loops, it is found to be proportionate to the code distance d within the red phase as shown in Fig. 5(a). By increasing the temperature, a transition point is anticipated where timelike Wilson loops become confined, concurrently with the proliferation of spacelike non-contractible

error strings. However, this threshold, which will be elucidated subsequently, does not encompass the correctability of measurement errors. Above this theoretical threshold, QEC is deemed ineffective, as evidenced by a persistent and finite logical error rate that is not ameliorated by enlarging the system size, particularly within the red phase depicted in Fig. 5(a).

Recall that confinement of spacelike Wilson loops is observed even below the theoretical threshold due to the fluctuation of timelike non-local error strings (Fig. 4(b)). Although those timelike error strings do not directly relate to logical Pauli operators, they signify the proliferation of measurement errors. Those non-local measurement errors (extending the whole time interval $[0, T]$ for any finite T) become indistinguishable from local Pauli errors and thus damage the decoding process. For example, the true syndrome of a single Pauli error string will be two non-local timelike strings starting from its boundary points. But in the meantime, the syndrome can be generated by non-local measurement errors, which may occur with a probability comparable to that of the Pauli string and are impervious to suppression by large T or large d . The consequence is that the decoder might mix up these two situations with a finite probability and inappropriately omit the correction of the aforementioned Pauli error. If this Pauli error anti-commutes with logical Z operators, the logical information will be damaged. Note that in this case, the defects caused by faulty measurement and Pauli error complements each other in the physical states, so the error cannot be detected even when applying more error correction cycles. In the low-temperature limit, we expect the logical error rate (measured with worst-case infidelity) to be proportional to the code distance, see Sec.SV of SI [55]. Given that the non-local timelike error strings consistently perforate the entire lattice, the choice of T in reality for decoding is inconsequential. Hence, the logical error rate is also not suppressed by increasing T . These results indicate the loss of quantum information.

Henceforth, our investigation elucidates crucial findings: Timelike non-local measurement errors and local Pauli errors together constitute a new mechanism that causes logical errors, and the probability of those events cannot be suppressed by large T or d . So when β_0 is finite, the QEC system behaves like it is above the true error threshold. Notice that the above mechanism is not explicit in the infinite time decoding scenario, since the non-local timelike syndromes are imagined to be connected by error strings at both the $t = +\infty$ and $t = -\infty$ ends, constituting complete world lines. This is not true in a realistic decoding process, because only finite error history can be taken into consideration.

This is in stark contrast to the case with only stochastic errors [29], where the perimeter law for both the spacelike and timelike Wilson loops guarantees the achievement of an effective error correction with a finite error history. Furthermore, it is worth noting that the RPGM [29] manifests an isotropic characteristic, i.e. the simultaneous deconfinement and confinement of the spacelike and timelike Wilson loops respectively, hence, obviating the need for distinct analyses of various error types.

In our case, the inability to correct measurement errors is

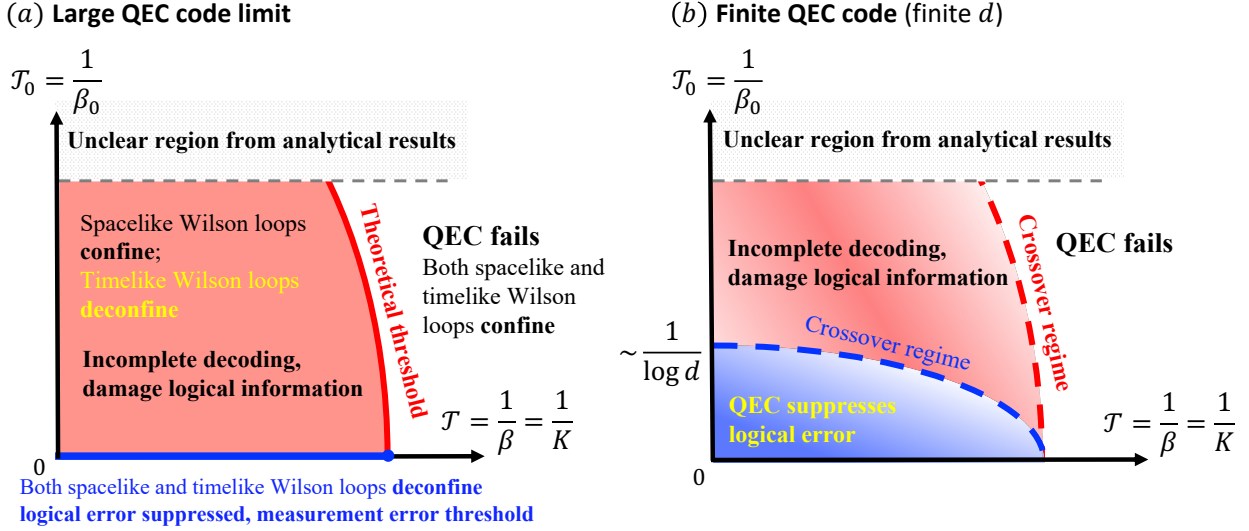


FIG. 5. (a) Our estimation of the phase structure in the thermodynamic limit $T \rightarrow +\infty$ and $N \rightarrow +\infty$ while setting $\mathcal{T} = 1/\beta = 1/K$ and $\mathcal{T}_0 = 1/\beta_0$. Above the theoretical threshold (red line) QEC fails due to non-contractible logical Pauli errors. Below the theoretical threshold and above the measurement error threshold (blue line), non-contractible logical Pauli errors are suppressed. However, measurement errors are still unidentifiable through decoding a finite error history and will be confounded with Pauli errors. Note that the \mathcal{T} axis where $\mathcal{T}_0 = 0$ represents the RPGM. While the theoretical threshold intersect with the \mathcal{T} axis at the common RPGM phase transition point [29], we are not sure yet whether it intersect with the \mathcal{T}_0 axis. Some details at higher temperatures still requires further investigation. (b) The phase diagram while fixing a finite code distance d . The phase transitions (thresholds) in Fig. 5(a) are smoothed into crossovers due to finite-size effect. Especially, the measurement error threshold becomes a finite-temperature crossover (blue dashed line), leading to a parameter region with a finite area (light blue region) that effectively suppresses logical errors. The parameters in this region should satisfy either Eq. (17) or Eq. (18) such that the non-local measurement errors will not be a problem. Specifically, the crossover condition $\mathcal{T}_0 \sim 1/\log d$ near the \mathcal{T}_0 axis is derived from Eq. (17) (However, Eq. (17) or Eq. (18) are only approximate expressions valid in the low-temperature limit. The precise value of this crossover still requires further investigation.). Increasing d , this region becomes smaller and smaller and eventually sticks to the \mathcal{T} axis. Above the crossover regime of measurement threshold in the light red region, the effect of non-local measurement errors on the QEC becomes non-negligible. As for the SM model side, the blue crossover detects the confinement of spacelike Wilson loops while the red crossover detects the confinement of timelike Wilson loops.

caused by the finite value of β_0 , i.e. the imperfection of initial state preparation; so we refer to $\beta_0 \rightarrow +\infty$ as the measurement error threshold of our error model. Setting $\beta = K$, a sketch of the phase diagram is shown in Fig. 5(a). In addition, a comparison between our error model and that with only stochastic errors [29] is shown in Tab. I.

For completeness, we scrutinize the phase structure in various limits. Notice that the red phase in Fig. 5(a) signifies the proliferation of measurement error strings, but logical errors result from a combination of measurement errors and Pauli errors. In the limit $K \rightarrow +\infty$ (keeping β_0 and β finite), the QEC protocol trivially succeeds as there will be no Pauli errors. But as long as K is finite, the logical error rate is not suppressed by the system size due to the indistinguishability between measurement errors and Pauli errors. In the scenario where $\beta \rightarrow +\infty$ but K and β_0 are finite, the non-local measurement errors are still present and cannot be decoded when intertwined with Pauli errors. As for the $\beta \rightarrow_0 +\infty$ limit, it reduces to the RPGM as mentioned before.

B. Finite-size effect

For a small code with limited system size N , we infer from Eq. (16) that the above problem might be circumvented with the limit

$$d \ll e^{\beta_0}, \quad (17)$$

or

$$d \ll [e^{4\beta_0}(e^{-4\beta} + e^{-4K} + 4e^{-2\beta-2K})]^{1/3}. \quad (18)$$

Here d is the code distance and $N = d^2$. The first bound is derived by assuming the areal term in Eq. (16) is negligible

$$e^{-4\beta_0} |\Pi(A)| (d^2 - |\Pi(A)|) \ll 1, \quad (19)$$

for all spacelike Wilson loops A . The left-hand-side maximizes when A is half the size of the spatial lattice $|\Pi(A)| = d^2/2$. Substituting $|\Pi(A)| = d^2/2$ into the above expression, we have

$$e^{-4\beta_0} d^4/4 \ll 1, \quad (20)$$

which is equivalent to Eq. (17) ignoring a constant factor. Physically, Eq. (17) is interpreted as the probability of the

	Our case	The case in Ref. [29]
Noise properties	1) coherent errors on entanglement gates of stabilizer measurement circuit (imperfect measurement), 2) stochastic Pauli errors on physical qubits	1) stochastic measurement errors of stabilizer measurement outcomes, 2) stochastic Pauli errors on physical qubits
Initial state	Affected by imperfect measurement during preparation (characterized by β_0)	Ideal toric code state
Error correction protocol	Multi-round syndrome measurement (number of rounds: T) and maximum likelihood decoder	
SM mapping	3-dimensional \mathbb{Z}_2 gauge model coupled to a 2-dimensional \mathbb{Z}_2 gauge model with quenched disorder	3-dimensional RPGM under Nishimori condition
Phase structure of SM model	When $\beta_0 \rightarrow +\infty$ (ideal initial state), the SM model reduces to RPGM. For finite β_0 (imperfect initial state), in the low-temperature phase (below theoretical threshold) timelike Wilson loops deconfine but spacelike Wilson loops confine; in the high-temperature phase (above theoretical threshold) all Wilson loops confine.	In the low-temperature phase (below theoretical threshold) all Wilson loops deconfine; in the high-temperature phase (above theoretical threshold) all Wilson loops confine.
Error correction performance	When $\beta_0 \rightarrow +\infty$ (ideal initial state), it is equivalent to the model in Ref. [29]. For finite β_0 (imperfect initial state), in the low-temperature phase (below theoretical threshold) there are still unidentifiable measurement errors that damage QEC performance, no matter how large T is; in the high-temperature phase (above theoretical threshold) QEC fails due to logical errors (non-contractible error loops).	In the low-temperature phase (below theoretical threshold), the probability of QEC success can be enlarged by increasing N and T (note that the QEC always fails while $T = 1$ but logical errors can be effectively suppressed while $T \gg \sqrt{N}$); in the high-temperature phase (above theoretical threshold) QEC fails.

TABLE I. Comparison between our case and the case with the stochastic measurement error model [29]. Note that although the measurement noises of the two models are different at the physical level, their error correction properties and corresponding SM models will become equivalent when we set the initial state in our model to be ideal ($\beta_0 \rightarrow +\infty$).

appearance of non-local measurement errors on the whole system is ignorable. The second bound is derived by considering the case when the perimetric decay is faster than the areal decay in Eq. (16) for a spacelike Wilson loop,

$$e^{-4\beta_0} |\Pi(A)|(d^2 - |\Pi(A)|) \ll (e^{-4\beta} + e^{-4K} + 4e^{-2\beta-2K}) |\partial A|_s. \quad (21)$$

Still we require A to be half of the spatial lattice, $|\Pi(A)| \sim d^2$ and $|\partial A|_s \sim d$. Thus we have

$$e^{-4\beta_0} d^4 \ll (e^{-4\beta} + e^{-4K} + 4e^{-2\beta-2K}) d, \quad (22)$$

which leads to Eq. (18). Physically, Eq. (18) is interpreted as the influence of non-local error strings is not significant compared to other local error strings. If either of these two bounds is satisfied, we anticipate that the ability of our QEC procedure to detect measurement errors will be similar to that of Ref. [29]. To do so, the imperfection of initial state preparation must be negligible or much smaller than the syndrome measurement imperfection and Pauli error rate. Even then the code distance is still upper bounded if we fix the error parameters β_0 , β and K . Usually, when performing QEC, we anticipate increasing code distance to suppress the logical error rate [30]. However, for the important error problem considered here, Eq. (17) and Eq. (18) form bounds that prevent the code from scaling up. Equivalently if we fix d and vary the error parameters, we obtain the phase diagram

in Fig. 5(b). It is noteworthy that the region enabling pragmatic error correction only experiences a gradual reduction as increasing the code distance, i.e. $\sim 1/\log d$, which is not excessively frustrating. In Sec.VII of SI [55], we describe a preparation procedure with the multiple-round measurement protocols that maintains decodability in small finite code systems.

VI. Relation to a realistic measurement circuit

In fact, the circuit shown in Fig. 1(b), which contains only two-qubit gates rather than a five-qubit evolution in our simple model, is more realistic, and it is expected to have worse performance while suffering from coherent noise on entanglement gates. Ref. [51] discussed an imperfect measurement model that mimics the behavior of superconducting quantum computation systems. The $CNOT$ gate is divided into a CZ gate and two Hadamard gates, $CNOT = H(CZ)H$ where H is the Hadamard gate acting on the target qubit (ancilla qubit in our setup). Each CZ gate is implemented by a time evolution

$$U = \exp \left[-i \frac{t}{4} (s^z \otimes \sigma_i^z - s^z \otimes I - I \otimes \sigma_i^z + I \otimes I) \right] \quad (23)$$

Here s labels the ancilla qubit and σ_i , $i = 1, 2, 3, 4$ labels the four data qubits. It recovers the CZ gate when $t = \pi$.

Assume the final ancilla measurement has an outcome $s = \pm 1$, the corresponding action on data qubits is

$$\begin{aligned}
 M_s = \langle s | H \exp \left[-i \frac{t}{4} \sum_i (s^z \otimes \sigma_i^z - s^z - \sigma_i^z + I) \right] H | 0 \rangle &= \frac{1}{2} \left(1 + se^{-i2t} \cos^4 \frac{t}{2} + se^{-i2t} \sin^4 \frac{t}{2} B_{p_0} \right) \\
 \times \left(1 - \frac{ise^{i2t} \sin \frac{t}{2} \cos^3 \frac{t}{2} + i \sin \frac{t}{2} \cos^7 \frac{t}{2} + i \sin^7 \frac{t}{2} \cos \frac{t}{2}}{(se^{i2t} + \cos^4 \frac{t}{2})^2 - \sin^8 \frac{t}{2}} \sum_i \sigma_i^z - \frac{\sin^2 \frac{t}{2} \cos^2 \frac{t}{2}}{se^{i2t} + \cos^4 \frac{t}{2} + \sin^4 \frac{t}{2}} \sum_{i < j} \sigma_i^z \sigma_j^z \right. \\
 \left. + \frac{ise^{i2t} \sin^3 \frac{t}{2} \cos \frac{t}{2} + i \sin^3 \frac{t}{2} \cos^5 \frac{t}{2} + i \sin^5 \frac{t}{2} \cos^3 \frac{t}{2}}{(se^{i2t} + \cos^4 \frac{t}{2})^2 - \sin^8 \frac{t}{2}} \sum_{i < j < k} \sigma_i^z \sigma_j^z \sigma_k^z \right). \quad (24)
 \end{aligned}$$

When $t = \pi$, one may check that the above expression reduces to the correct projection $(I + sB_{p_0})/2$. When $t \neq \pi$, M_s stands for an imperfect measurement operator.

To understand the effect of the realistic error model Eq. (24), we compare it with the simplified model Eq. (3). As a picture of how decoding fails for imperfect initial states, recall that those states contain superpositions of defects (stabilizer generator = -1 components) whose amplitudes do not decay with the distance between defects. The consequence is that the failure probability of decoding will not decay with code distance. We notice that in its expression the first factor $1 + se^{-i2t} \cos^4(t/2) + se^{-i2t} \sin^4(t/2)B_{p_0}$ is similar to the imperfect measurement operator discussed in Eq. (3) $\exp(\beta s_{p_0} B_{p_0}/2) = \cosh(\beta/2) + s_{p_0} \sinh(\beta/2)B_{p_0}$. Recall that in the simple model depicted in Fig. 1(c), the absence of a finite measurement error threshold is attributed to the superposition of defects with $B_{p_0} = -1$. The amplitudes of these defects remain constant regardless of their spatial separation and depend solely on their quantity. In contrast, the realistic model illustrated in Fig. 1(b) incorporates the term $\exp(\beta s_{p_0} B_{p_0}/2)$. This inclusion leads to superpositions analogous to those in the simple model, thereby suggesting that the issue of lacking a finite threshold persists in the realistic scenario. Furthermore, there is an additional factor, which can be viewed as coherent errors appearing on data qubits. These coherent will further lead to $A_v = -1$ defects in the initial code state (see Sec. SVIII of SI). So while discussing error correction, aside from the previously discussed consequences, coherent errors are likely to inflict greater damage on the error correction process, resulting in deteriorated performance. We also notice that under this realistic measurement model, if we define logical states by applying logical operators to the imperfect initial state, those states will not be orthogonal to each other, making it much harder to solve exactly. Finally, we stress that the preceding discussion concerning the realistic model relies on model-based calculations and partially qualitative reasoning. A rigorous mathematical proof for general cases is essential and merits comprehensive investigation in future studies.

For a small finite code, when considering the application of the multi-round measurement preparation protocol to specific logical states within the Pauli basis, its effectiveness is brought into question for more realistic measurement cir-

cuits. In this scenario, the implementation of the A_{v_0} measurement is necessitated for the correction of the Z coherent error strings induced by the B_{p_0} measurement. Given that these two distinct types of imperfect stabilizer measurement operators are non-commutative, their resulting measurement outcomes are inherently interdependent. Future investigations could benefit from exploring a hybrid decoding approach that combines both A_{v_0} and B_{p_0} stabilizer measurement data.

VII. Discussions

We study the performance of toric code QEC under the influence of various important error types, including imperfect measurement circuits for both preparation and error detection, as well as the qubit-level stochastic Pauli noise. We establish a connection between the corresponding QEC performance and a novel statistical mechanical model. Our statistical mechanical analysis reveals the mechanism of how the imperfect initial code states affect the following error correction cycle. We emphasize that the code state preparation requires special attention, which was rarely discussed in previous theoretical studies of QEC error thresholds. A naive preparation protocol could destroy the ability to shield quantum information from local Pauli perturbations. Although focusing on toric code in the calculations, we expect our results hold for general boundary conditions of large enough surface codes since they are not expect to affect the qualitative properties of the SM model in the thermodynamic limit. In addition, we mention that QEC code states could be prepared by pure unitaries instead of measurements [21, 64, 65]. However in large systems, the typical circuit depth of unitary preparation is larger than measurement preparation in the ideal case, and its resilience against coherent deviations could be even worse.

Before closure, it is important to highlight that our results indicate a different impact based on the scale of quantum codes. Specifically, smaller quantum codes, typically situated within the $1/\log d$ threshold, still exhibit resilience against the outlined challenges (Sec.SVII of SI [55]), thereby maintaining robust QEC capabilities. Current small-scale experiments of surface code QEC [6, 17, 18, 20, 21, 25] are be-

lieved to stay in the effectively correctable region such that they provides positive results. Conversely, our findings hold considerable significance for larger-scale systems, which are central to the realization of application-level fault-tolerant quantum computing. As the scale of the system expands, the criticality of code space preparation must be significantly intensified, accompanied by an increased consumption of resources. This observation emphasizes the crucial need for a focus on refining state preparation protocols, a measure essential to safeguarding the efficacy and feasibility of QEC for advanced fault-tolerant quantum computations.

Acknowledgments

Authors thank Guo-Yi Zhu for the discussions on the finite-size effect of the SM model, and Kenneth Brown for

pointing out the state preparation with the multiple-round measurement protocols. We thank Jing-Yuan Chen, Ying-Fei Gu, Xie Chen, Guanyu Zhu, Ying Li, Li Rao, and Qinghong Yang for helpful discussions. This work is supported by National Natural Science Foundation of China (Grants No. 92365111), the Innovation Program for Quantum Science and Technology (Grant No. 2021ZD0302400) and Beijing Natural Science Foundation (Grant No. Z220002).

Competing interests

The authors declare no competing interests.

Data availability

Data sharing is not applicable to this article, as no datasets were generated or analyzed during the current study.

-
- [1] F. Arute, K. Arya, R. Babbush, and et al., *Nature* **574** (2019), [10.1038/s41586-019-1666-5](https://doi.org/10.1038/s41586-019-1666-5).
- [2] H.-S. Zhong, H. Wang, Y.-H. Deng, and et al., *Science* **370**, 1460 (2020).
- [3] Y. Wu, W.-S. Bao, S. Cao, and et al., *Phys. Rev. Lett.* **127**, 180501 (2021).
- [4] F. Arute, K. Arya, R. Babbush, and et al., *Science* **369**, 1084 (2020).
- [5] M. Gong, S. Wang, C. Zha, and et al., *Science* **372**, 948 (2021).
- [6] A. Erhard, H. Poulsen Nautrup, M. Meth, L. Postler, R. Stricker, M. Stadler, V. Negnevitsky, M. Ringbauer, P. Schindler, H. J. Briegel, R. Blatt, N. Friis, and T. Monz, *Nature* **589**, 220 (2021).
- [7] J. M. Pino, J. M. Dreiling, C. Figgatt, and et al., *Nature* **592**, 209 (2021).
- [8] C. Ryan-Anderson, J. G. Bohnet, K. Lee, D. Gresh, A. Hankin, J. P. Gaebler, D. Francois, A. Chernoguzov, D. Lucchetti, N. C. Brown, T. M. Gatterman, S. K. Halit, K. Gilmore, J. A. Gerber, B. Neyenhuis, D. Hayes, and R. P. Stutz, *Phys. Rev. X* **11**, 041058 (2021).
- [9] J. Preskill, *Quantum* **2**, 79 (2018).
- [10] P. W. Shor, *Phys. Rev. A* **52**, R2493 (1995).
- [11] A. Steane, *Proc. R. Soc. Lond. A* **452**, 2551 (1996).
- [12] A. R. Calderbank and P. W. Shor, *Phys. Rev. A* **54**, 1098 (1996).
- [13] P. Schindler, J. T. Barreiro, T. Monz, V. Nebendahl, D. Nigg, M. Chwalla, M. Hennrich, and R. Blatt, *Science* **332**, 1059 (2011).
- [14] D. Nigg, M. Müller, E. A. Martinez, P. Schindler, M. Hennrich, T. Monz, M. A. Martin-Delgado, and R. Blatt, *Science* **345**, 302 (2014).
- [15] N. Ofek, A. Petrenko, R. Heeres, P. Reinhold, Z. Leghtas, B. Vlastakis, Y. Liu, L. Frunzio, S. M. Girvin, L. Jiang, M. Mirrahimi, M. H. Devoret, and R. J. Schoelkopf, *Nature* **536**, 441 (2016).
- [16] L. Hu, Y. Ma, W. Cai, X. Mu, Y. Xu, W. Wang, Y. Wu, H. Wang, Y. P. Song, C. L. Zou, S. M. Girvin, L.-M. Duan, and L. Sun, *Nature Physics* **15**, 503 (2019).
- [17] C. K. Andersen, A. Remm, S. Lazar, S. Krinner, N. Lacroix, G. J. Norris, M. Gabureac, C. Eichler, and A. Wallraff, *Nature Physics* **16**, 875 (2020).
- [18] G. Q. Ai, *Nature* **595**, 383 (2021).
- [19] Y.-H. Luo, M.-C. Chen, M. Erhard, H.-S. Zhong, D. Wu, H.-Y. Tang, Q. Zhao, X.-L. Wang, K. Fujii, L. Li, N.-L. Liu, K. Nemoto, W. J. Munro, C.-Y. Lu, A. Zeilinger, and J.-W. Pan, *Proceedings of the National Academy of Sciences* **118**, e2026250118 (2021).
- [20] J. F. Marques, B. M. Varbanov, M. S. Moreira, H. Ali, N. Muthusubramanian, C. Zachariadis, F. Battistel, M. Beekman, N. Haider, W. Vlothuizen, A. Bruno, B. M. Terhal, and L. DiCarlo, *Nature Physics* **18**, 80 (2022).
- [21] Y. Zhao, Y. Ye, H.-L. Huang, Y. Zhang, D. Wu, H. Guan, Q. Zhu, Z. Wei, T. He, S. Cao, F. Chen, T.-H. Chung, H. Deng, D. Fan, M. Gong, C. Guo, S. Guo, L. Han, N. Li, S. Li, Y. Li, F. Liang, J. Lin, H. Qian, H. Rong, H. Su, L. Sun, S. Wang, Y. Wu, Y. Xu, C. Ying, J. Yu, C. Zha, K. Zhang, Y.-H. Huo, C.-Y. Lu, C.-Z. Peng, X. Zhu, and J.-W. Pan, *Phys. Rev. Lett.* **129**, 030501 (2022).
- [22] C. Ryan-Anderson, J. G. Bohnet, K. Lee, D. Gresh, A. Hankin, J. P. Gaebler, D. Francois, A. Chernoguzov, D. Lucchetti, N. C. Brown, T. M. Gatterman, S. K. Halit, K. Gilmore, J. A. Gerber, B. Neyenhuis, D. Hayes, and R. P. Stutz, *Phys. Rev. X* **11**, 041058 (2021).
- [23] L. Egan, D. M. Debroy, C. Noel, A. Risinger, D. Zhu, D. Biswas, M. Newman, M. Li, K. R. Brown, M. Cetina, and C. Monroe, “Fault-tolerant operation of a quantum error-correction code,” (2020), [arXiv:2009.11482](https://arxiv.org/abs/2009.11482) [quant-ph].
- [24] N. Sundaresan, T. J. Yoder, Y. Kim, M. Li, E. H. Chen, G. Harper, T. Thorbeck, A. W. Cross, A. D. Córcoles, and M. Takita, *Nature Communications* **14**, 2852 (2023).
- [25] D. Bluvstein, S. J. Evered, A. A. Geim, S. H. Li, H. Zhou, T. Manovitz, S. Ebadi, M. Cain, M. Kalinowski, D. Hangleiter, J. P. Bonilla Ataides, N. Maskara, I. Cong, X. Gao, P. Sales Rodriguez, T. Karolyshyn, G. Semeghini, M. J. Gullans, M. Greiner, V. Vuletić, and M. D. Lukin, *Nature* **626**, 58 (2024).
- [26] E. Knill, R. Laflamme, and W. Zurek, *Proc. R. Soc. Lond. A* **454** (1998).
- [27] D. Aharonov and M. Ben-Or, “The role of correlated noise in quantum computing,” (1999), [arXiv:9906129](https://arxiv.org/abs/9906129) [quant-ph].
- [28] P. Aliferis, D. Gottesman, and J. Preskill, *Quant. Inf. Comput.* **6**, 97 (2006).
- [29] E. Dennis, A. Kitaev, A. Landahl, and J. Preskill, *Journal of Mathematical Physics* **43**, 4452 (2002).
- [30] A. G. Fowler, M. Mariantoni, J. M. Martinis, and A. N. Cleland, *Phys. Rev. A* **86**, 032324 (2012).
- [31] A. A. Kovalev and L. P. Pryadko, *Physical Review A* **87**,

- 020304 (2013).
- [32] D. Gottesman, “Fault-Tolerant Quantum Computation with Constant Overhead,” (2014), arXiv:1310.2984 [quant-ph].
- [33] H. Bombin, “An introduction to topological quantum codes,” (2013), arXiv:1311.0277 [quant-ph].
- [34] C. Vuillot, H. Asasi, Y. Wang, L. P. Pryadko, and B. M. Terhal, *Physical Review A* **99**, 032344 (2019), arXiv:1810.00047 [quant-ph].
- [35] P. Baireuther, M. D. Caio, B. Criger, C. W. J. Beenakker, and T. E. O’Brien, *New Journal of Physics* **21**, 013003 (2019).
- [36] L. P. Pryadko, *Quantum* **4**, 304 (2020), arXiv:1909.06732 [quant-ph].
- [37] D. Aharonov, A. Kitaev, and J. Preskill, *Phys. Rev. Lett.* **96**, 050504 (2006).
- [38] C. T. Chubb and S. T. Flammia, *Ann. Inst. Henri Poincaré Comb. Phys. Interact.* **8** (2021), 10.4171/AIHPD/105.
- [39] E. Novais, E. R. Mucciolo, and H. U. Baranger, *Phys. Rev. Lett.* **98**, 040501 (2007).
- [40] E. Novais, E. R. Mucciolo, and H. U. Baranger, *Phys. Rev. A* **78**, 012314 (2008).
- [41] J. P. Barnes, C. J. Trout, D. Lucarelli, and B. D. Clader, *Phys. Rev. A* **95**, 062338 (2017).
- [42] S. J. Beale, J. J. Wallman, M. Gutiérrez, K. R. Brown, and R. Laflamme, *Phys. Rev. Lett.* **121**, 190501 (2018).
- [43] S. Bravyi, M. Englbrecht, R. König, and N. Peard, *npj Quantum Information* **4** (2018), 10.1038/s41534-018-0106-y.
- [44] J. K. Iverson and J. Preskill, *New Journal of Physics* **22**, 073066 (2020).
- [45] E. Huang, A. C. Doherty, and S. Flammia, *Phys. Rev. A* **99**, 022313 (2019).
- [46] Z. Cai, X. Xu, and S. C. Benjamin, *npj Quantum Information* **6** (2020), 10.1038/s41534-019-0233-0.
- [47] Y. Ouyang, *npj Quantum Information* **7** (2021), 10.1038/s41534-021-00429-8.
- [48] Y. Zhao and D. E. Liu, “An analytic study of the independent coherent errors in the surface code,” (2021), arXiv:2112.00473 [quant-ph].
- [49] F. Venn, J. Behrends, and B. Béri, *Phys. Rev. Lett.* **131**, 060603 (2023).
- [50] D. Debroy, M. Li, M. Newman, and K. R. Brown, *Physical Review Letters* **121**, 250502 (2018), arxiv:1810.01040 [quant-ph].
- [51] Q. Yang and D. E. Liu, *Physical Review A* **105**, 022434 (2022).
- [52] G.-Y. Zhu, N. Tantivasadakarn, A. Vishwanath, S. Trebst, and R. Verresen, *Phys. Rev. Lett.* **131**, 200201 (2023).
- [53] A. Kitaev, *Annals of Physics* **303**, 2 (2003).
- [54] R. Acharya, I. Aleiner, R. Allen, and et al., “Suppressing quantum errors by scaling a surface code logical qubit,” (2022), arXiv:2207.06431 [quant-ph].
- [55] See Supplemental Information for details of the derivation.
- [56] J. Y. Lee, W. Ji, Z. Bi, and M. P. A. Fisher, “Decoding measurement-prepared quantum phases and transitions: from ising model to gauge theory, and beyond,” (2022), arXiv:2208.11699 [cond-mat.str-el].
- [57] S. Sang, Y. Zou, and T. H. Hsieh, “Mixed-state Quantum Phases: Renormalization and Quantum Error Correction,” (2023), arxiv:2310.08639.
- [58] J. Yi, W. Ye, D. Gottesman, and Z.-W. Liu, “Complexity and order in approximate quantum error-correcting codes,” (2023), arxiv:2310.04710 [cond-mat, physics:hep-th, physics:math-ph, physics:quant-ph].
- [59] F. J. Wegner, *Journal of Mathematical Physics* **12**, 2259 (1971).
- [60] J. B. Kogut, *Rev. Mod. Phys.* **51**, 659 (1979).
- [61] C. Wang, J. Harrington, and J. Preskill, *Annals of Physics* **303**, 31 (2003).
- [62] T. Ohno, G. Arakawa, I. Ichinose, and T. Matsui, *Nuclear Physics B* **697**, 462 (2004).
- [63] H. Nishimori, *Progress of Theoretical Physics* **66**, 1169 (1981).
- [64] N. M. Linke, M. Gutierrez, K. A. Landsman, C. Figgatt, S. Debnath, K. R. Brown, and C. Monroe, *Science Advances* **3**, e1701074 (2017), <https://www.science.org/doi/pdf/10.1126/sciadv.1701074>.
- [65] M. Takita, A. W. Cross, A. D. Córcoles, J. M. Chow, and J. M. Gambetta, *Physical Review Letters* **119**, 180501 (2017).

VULNERABILITY OF FAULT-TOLERANT TOPOLOGICAL QUANTUM ERROR CORRECTION TO QUANTUM DEVIATIONS IN CODE SPACE

In this supplemental information, we provide details about derivations of the results in the main text. In Sec. [S](#) we discuss some properties about code space when initial state preparation suffers from imperfection measurement. In Sec. [SII](#) we derive the SM mapping explicitly. In Sec. [SIII](#) we talk about the consequence of local symmetry under the Nishimori condition. In Sec. [SIV](#) we derive the low-temperature expansion of the Wilson loop. In Sec. [SV](#) we examine the behavior of logical error rate in the low-error-rate limit. In Sec. [SVI](#) we have a simple discussion on the case where the coherent deviation in the imperfect measurement model is IID instead of fixed to a specific value. In Sec. [SVII](#), we provide a code state preparation procedure to stay in the decodable region for finite codes. In Sec. [SVIII](#), we discuss the imperfect code state under the assumption of the realistic measurement circuit.

SI. CODE SUBSPACE UNDER IMPERFECT MEASUREMENT

Here we discuss the imperfect code subspace under the presence of coherent errors on entanglement gates during state preparation. Starting with a product state $\bigotimes_{e_0} |+\rangle_{e_0}$, we obtain the (unnormalized) state $M_{\{s_{p_0}\}} \bigotimes_{e_0} |+\rangle_{e_0}$ with probability

$$P(\{s_{p_0}\}) = \bigotimes_{e_0} \langle + |_{e_0} E_{\{s_{p_0}\}} \bigotimes_{e_0} | + \rangle_{e_0} = \frac{1}{(8 \cosh \beta)^N} \mathcal{Z}_{\{s_{p_0}\}}, \quad (\text{S1})$$

$$\mathcal{Z}_{\{s_{p_0}\}} = \sum_{\{\sigma_{e_0}\}} \exp \left[\beta \sum_{p_0} s_{p_0} b_{p_0} \right], b_{p_0} = \prod_{e_0 \in \partial p_0} \sigma_{e_0}, \quad (\text{S2})$$

where $M_{\{s_{p_0}\}}$ is the imperfect measurement operator

$$M_{\{s_{p_0}\}} = \frac{1}{(\sqrt{2} \cosh \beta)^N} \exp \left[\frac{1}{2} \beta \sum_{p_0} s_{p_0} B_{p_0} \right], \quad (\text{S3})$$

and $E_{\{s_{p_0}\}} = M_{\{s_{p_0}\}}^\dagger M_{\{s_{p_0}\}}$ is the corresponding POVM operator. By expanding $\bigotimes_{e_0} |+\rangle_{e_0}$ under computational basis $\bigotimes_{e_0} |+\rangle_{e_0} = (1/2^N) \sum_{\{\sigma_{e_0}\}} \bigotimes_{e_0} |\sigma_{e_0}\rangle$, where $\sigma_{e_0} = \pm 1$ is the eigenvalue of Pauli operator Z_{e_0} , it can be shown that $P(\{s_{p_0}\})$ is proportional to the partition function of a 2-d \mathbb{Z}_2 lattice gauge theory $\mathcal{Z}_{\{s_{p_0}\}}$ [[1](#), [2](#)], which is a useful method to dealing with the post-measurement state and is helpful to our following derivations. Note that 2-d \mathbb{Z} lattice gauge theory is exact-solvable [[3](#)]. By noticing that the Boltzmann weight only depends on the value of b_{p_0} , we rewrite the summation of spin configurations as a summation of b_{p_0} configurations together with 1-form symmetry operations

$$\sum_{\{\sigma_{e_0}\}} = \sum_{\{b_{p_0}\}} \delta_{\prod_{p_0} b_{p_0}, 1} \sum_{\text{dual loop}} \cdot \quad (\text{S4})$$

here $\delta_{\prod_{p_0} b_{p_0}, 1}$ means that the product of all b_{p_0} must equal to 1, since the lattice is embedded in a torus surface. We may check the degree of freedoms involved in the summation $2^{2N} = 2^N/2 \times 2^{N+1}$. Thus we have

$$\begin{aligned}
\mathcal{Z}_{\{s_{p_0}\}} &= \sum_{\{b_{p_0}\}} \delta_{\prod_{p_0} b_{p_0}, 1} \sum_{\text{dual loop}} \exp \left[\beta \sum_{p_0} s_{p_0} b_{p_0} \right] \\
&= 2^{N+1} \sum_{\{b_{p_0}\}} \frac{1 + \prod_{p_0} b_{p_0}}{2} \exp \left[\beta \sum_{p_0} s_{p_0} b_{p_0} \right] \\
&= 2^N \prod_p \left(\sum_{b_{p_0}} \exp [\beta s_{p_0} b_{p_0}] + \sum_{b_{p_0}} b_{p_0} \exp [\beta s_{p_0} b_{p_0}] \right) \\
&= 2^N (2 \cosh \beta)^N + 2^N (2 \sinh \beta)^N \prod_{p_0} s_{p_0},
\end{aligned} \tag{S5}$$

and hence we have the probability of measurement outcomes

$$P(\{s_{p_0}\}) = \frac{1 + (\tanh \beta)^N \prod_p s_{p_0}}{2^N}. \tag{S6}$$

Note that $\prod_{p_0} s_{p_0}$ is the parity of $\{s_{p_0}\}$ configuration.

From the above discussion, it can be seen that we might get different states with respect to the ancilla measurement outcome $\{s_{p_0}\}$. But we will fix the initial state as $M_{\{+\}} \otimes_{e_0} |+\rangle_{e_0}$, where we assumed the measurement outcome of ancilla qubits are all +1. For other measurement outcomes $\{s_{p_0}\}$, we can redefine the sign of our stabilizer $B_{p_0} \rightarrow s_{p_0} B_{p_0}$ in order that the following discussions still apply. The only thing we should take into consideration is the parity of outcome $\{s_{p_0}\}$ because under the redefinition $\prod_{p_0} B_{p_0} = 1 \rightarrow \prod_{p_0} B_{p_0} = \prod_s s_{p_0}$ and we will get -1 for odd parity. In the odd parity case, the defects on the lattice cannot be paired up. We cannot redefine an odd number of B_{p_0} 's and still satisfy the constrain $\prod_{p_0} B_{p_0} = 1$, and start QEC with a state where defects already present won't be a benefit to the performance. Hence we ignore odd parity outcomes. We might consider it as a post-selection procedure, which chooses the even parity result that occurs with probability $P_+ = (1 + (\tanh \beta)^N)/2$, see Eq. (S6). We find that $1/2 \leq P_+ \leq 1$ for $0 \leq \beta \leq +\infty$. Note that this probability is close to 1 when β is sufficiently large, so the post-selection procedure is reasonable for experimental consideration.

Till now we have only obtained one logical state. What about other states in the imperfect code subspace? The problem is that the matrix rank of $M_{\{s_{p_0}\}}$ is 2^{2N} , which means that if we view it as a map defined on the whole 2^{2N} dimensional Hilbert space of physical qubits, $M_{\{s_{p_0}\}} : \mathcal{H} \rightarrow \mathcal{H}$, then we find that $\text{Im}(M_{\{s_{p_0}\}}) = \mathcal{H}$. This is different from the projective measurement case that $P_{\{s_{p_0}\}} = \prod_{p_0} (I + s_{p_0} B_{p_0})/2$ projects any states into the $B_{p_0} = s_{p_0}$ subspace. That is why we define the code space using logical operators in analogy to experimental setups. In summary, our four logical basis states are defined as

$$\begin{aligned}
|\widetilde{++}\rangle &= \frac{M_{\{+\}} \otimes_{e_0} |+\rangle_{e_0}}{\sqrt{\otimes_{e_0} \langle +|_{e_0} M_{\{+\}}^\dagger M_{\{+\}} \otimes_{e_0} |+\rangle_{e_0}}}, \\
|\widetilde{+-}\rangle &= Z_{l_1} |\widetilde{++}\rangle, \quad |\widetilde{-+}\rangle = Z_{l_2} |\widetilde{++}\rangle, \quad |\widetilde{--}\rangle = Z_{l_1} Z_{l_2} |\widetilde{++}\rangle,
\end{aligned} \tag{S7}$$

Notice that $|\widetilde{++}\rangle$ state correspond to the model

$$\mathcal{Z}_{\{+\}} = \sum_{\{\sigma_{e_0}\}} \exp \left[\beta \sum_{p_0} b_{p_0} \right]. \tag{S8}$$

Given the above imperfect logical states, the expectation value of Pauli Z operators can be computed through the classical SM model [1, 2]. We denote $\langle \cdot \rangle_{\{+\}}^q$ as the expectation value of the post-measurement state $|\widetilde{++}\rangle$, then

$$\left\langle \prod_{e_0 \in c_0} Z_{e_0} \right\rangle_{\{+\}}^q = \left\langle \prod_{e_0 \in c_0} \sigma_{e_0} \right\rangle_{\{+\}}^c. \tag{S9}$$

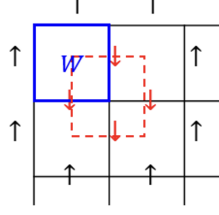


FIG. S1. 2-d \mathbb{Z}_2 lattice gauge theory. The classical spins σ_{e_0} are associated with each edge. Both the Hamiltonian and Wilson loop (blue solid loop) are invariant under 1-form symmetry operation (red dashed loop) which flips the spins on a dual loop.

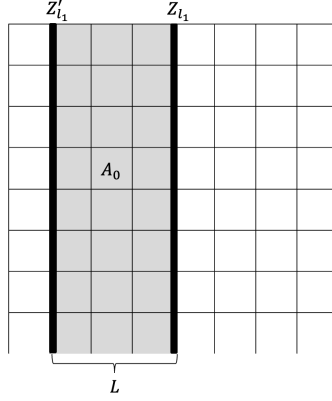


FIG. S2. Different definitions of logical Pauli Z operator. Under imperfect measurement preparation, the two logical states defined by them are different. The fidelity between these two states relates to the expectation value of a Wilson loop observable constituted by these two non-contractible loops.

where we denote c_0 as a set of several edges and $\langle \cdot \rangle_{\{+\}}^c$ as the expectation value of the classical model $\mathcal{Z}_{\{+\}}$.

2-d \mathbb{Z}_2 lattice gauge theory possesses 1-form symmetry [3]. As in Fig. S1, if we flip all the spins along a dual loop l_1^* it does not change the value of b_{p_0} on any plaquette p_0 , hence does not change the partition function, i.e. Eq. (S2).

For 2-d \mathbb{Z}_2 lattice gauge theory, Elitzur's theorem [3, 4] states that the expectation value of any observable that varies under 1-form symmetry operation vanishes (even under the presence of infinitesimal source term). For example consider the overlap between two logical states

$$\langle \widetilde{-+} | \widetilde{++} \rangle = \langle \widetilde{++} | Z_{l_1} | \widetilde{++} \rangle = \langle Z_{l_1} \rangle_{\{+\}}^c = \left\langle \prod_{e_0 \in l_1} \sigma_{e_0} \right\rangle_{\{+\}}^c. \quad (\text{S10})$$

The operator $\prod_{e_0 \in l_1} \sigma_{e_0}$ is the product σ_{e_0} spins that wind around the non-contractible loop l_1 , and it changes sign under the 1-form symmetry operation that flips the spins on a dual non-contractible loop l_1^* that intersect with l_1 . Consequently, we find that $\langle \widetilde{-+} | \widetilde{++} \rangle = 0$. Note that this result can also be checked through explicit calculation since $\mathcal{Z}_{\{+\}}$ acquires an exact solution. Similarly, we find that all the four states $\{|\widetilde{++}\rangle, |\widetilde{-+}\rangle, |\widetilde{+-}\rangle, |\widetilde{--}\rangle\}$ are orthogonal to each other. Therefore, they form an orthonormal basis of a 4 dimensional subspace. This justifies our definition of the imperfect code subspace

$$\widetilde{\mathcal{C}}(\beta) = \text{span}\{|\widetilde{++}\rangle, |\widetilde{-+}\rangle, |\widetilde{+-}\rangle, |\widetilde{--}\rangle\} \quad (\text{S11})$$

What is more, these four states are still eigenstates of logical X operators. Since $X_{l_1^*}, X_{l_2^*}$ commute with imperfect measurement operator $M_{\{+\}}$ and act as 1 on the initial product state, we find that $X_{l_1^*} |\widetilde{++}\rangle = |\widetilde{++}\rangle, X_{l_2^*} |\widetilde{++}\rangle = |\widetilde{++}\rangle$. The act on the other three states is determined by the commutation relation between logical X and logical Z . Note that these properties are not universal for imperfect measurement but depend on the specific measurement protocol.

Here we point out that, unlike the projective measurement case, $\widetilde{\mathcal{C}}$ depends on the choice of logical operators on the lattice. For example, consider a different choice of logical Z operator Z'_{l_1} as in Fig. S2. We can calculate the fidelity

between $|-\rangle$ and the new state defined by the new logical operator $|-\rangle = Z'_{l_1} |+\rangle$:

$$\langle \widetilde{-+} | \widetilde{-+} \rangle' = \langle \widetilde{++} | Z_{l_1} Z'_{l_1} | \widetilde{++} \rangle = \langle Z_{l_1} Z'_{l_1} \rangle_{\{+\}}^q \quad (\text{S12})$$

Note that $Z_{l_1} Z'_{l_1}$ forms a Wilson loop that could be written as the boundary of a region A . For the classical model, Wilson loops are 1-form symmetry invariant observables and acquire non-zero expectation values. For example consider the Wilson loop

$$W_{A_0} = \prod_{p_0 \in A_0} b_{p_0} = \prod_{e_0 \in \partial A_0} \sigma_{e_0}, \quad (\text{S13})$$

where A_0 is a 2-d region (a set of plaquettes) and ∂A_0 is the set of edges at the boundary of A_0 . Its expectation value can be evaluated similarly as the partition function, which leads to

$$\langle W_{A_0} \rangle_{\{+\}}^c = \frac{(\tanh \beta)^{|A_0|} + (\tanh \beta)^{N-|A_0|}}{1 + (\tanh \beta)^N}. \quad (\text{S14})$$

With the help of Eq. (S14), we obtain:

$$\langle \widetilde{-+} | \widetilde{-+} \rangle' = \frac{(\tanh \beta)^{dL} + (\tanh \beta)^{N-dL}}{1 + (\tanh \beta)^N} \quad (\text{S15})$$

which is smaller than 1 for finite β , implies that the two states are different.

In addition, notice that we can take the product of the eigenstates of $N-1$ B_{p_0} operators, $N-1$ A_{v_0} operators and 2 logical operators $X_{l_1^*}$ and $X_{l_2^*}$ to form a complete basis of the whole Hilbert space of physical qubits. Under this basis the product $|+\rangle$ state can be written as

$$\bigotimes_{e_0} |+\rangle_{e_0} = \bigotimes_{p_0}' \sum_{b_{p_0}=\pm} |B_{p_0} = b_{p_0}\rangle \bigotimes_{v_0}' |A_{v_0} = +\rangle \bigotimes |X_{l_1^*} = +\rangle \bigotimes |X_{l_2^*} = +\rangle, \quad (\text{S16})$$

Here the prime on the product symbol means that a chosen plaquette or vertex is excluded to satisfy the global constraint $\prod_{p_0} B_{p_0} = \prod_{v_0} A_{v_0} = I$. This formula is verified as follows. Since the action of A_{v_0} 's and logical X operators on $\bigotimes_{e_0} |+\rangle_{e_0}$ all yield +1, the state must be the +1 eigenstate of these operators. Besides, assume the excluded plaquette is f_0 . Consider a Pauli X string $X_{(f_0 \rightarrow q_0)}$ that starts at f_0 and ends at some other plaquette q_0 . Since $X_{(f_0 \rightarrow q_0)}$ commutes with all $N-1$ A_{v_0} operators, logical X operators and $N-2$ B_{p_0} 's with $p_0 \neq q_0, f_0$, it only acts on the factor $|B_{q_0} = \pm\rangle$ under the above basis. Note that $X_{(f_0 \rightarrow q_0)}$ anti-commutes with B_{q_0} , so $X_{(f_0 \rightarrow q_0)} |B_{q_0} = \pm\rangle = |B_{q_0} = \mp\rangle$. Since $X_{(f_0 \rightarrow q_0)} \bigotimes_{e_0} |+\rangle_{e_0} = \bigotimes_{e_0} |+\rangle_{e_0}$, the product state must be stabilized by $X_{(f_0 \rightarrow q_0)}$. Applying such strings to all the plaquettes, we find that $\bigotimes_{e_0} |+\rangle_{e_0}$ is the +1 eigenstate of $X_{(f_0 \rightarrow q_0)}$ for all $q_0 \neq f_0$, which leads to Eq. (S16). With the above considerations, we find that the imperfect measurement operator $M_{\{s_{p_0}\}}$ only acts on the stabilizer bits ($|B_{p_0} = \pm\rangle$ and $|A_{v_0} = \pm\rangle$) and logical operators only act on the logical bits ($|X_{l_1^*} = \pm\rangle$ and $|X_{l_2^*} = \pm\rangle$). Consequently, any state $|\tilde{\Psi}\rangle$ in the code space $\tilde{\mathcal{C}}$ can be expanded under the stabilizer basis to achieve the form:

$$|\tilde{\Psi}\rangle \propto \left[\exp\left(\frac{\beta}{2} \prod_{p_0}' B_{p_0}\right) \bigotimes_{p_0}' \sum_{b_{p_0}=\pm} \exp\left(\frac{\beta}{2} b_{p_0}\right) |B_{p_0} = b_{p_0}\rangle \right] \left[\bigotimes_{v_0}' |A_{v_0} = +\rangle \right] \bigotimes |L\rangle, \quad (\text{S17})$$

where $|L\rangle$ represents the logical qubits and is exactly where the logical information is stored.

III. DERIVATION OF STATISTICAL MECHANICAL MAPPING

Recall that we have considered a multi-round error correction protocol [5] under imperfect syndrome measurement stated as follows:

1. Start with an arbitrary state $|\tilde{\Psi}\rangle$ in $\tilde{\mathcal{C}}(\beta_0)$.
2. Probabilistic Pauli X error acts at each integer valued time $t = 1, 2, \dots, T$. The X error at each physical qubit on each time slice occurs independently with probability q . Denote the error configuration at time t as $\{\eta_{e_0}(t)\}$

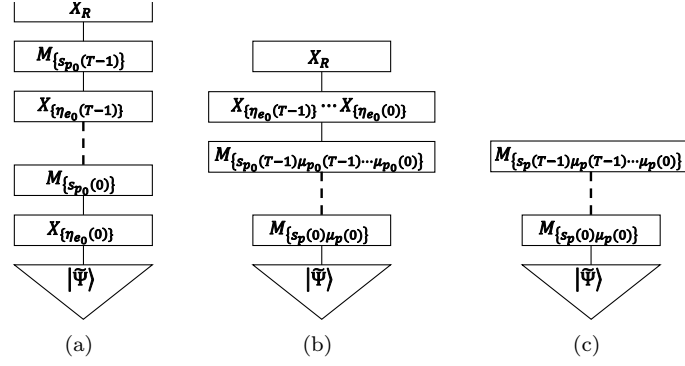


FIG. S3. Diagrams for error correction procedure. The bottom triangle is the initial state. The squares above represent action of Pauli errors and imperfect measurements. (a) Original error correction procedure. Pauli errors and imperfect measurement act repetitiously. (b) Move Pauli error operators to the top making use of the commutation relation, i.e. Eq. (S18). (c) When the correction operator and Pauli error operators form a stabilizer, they together commute with imperfect measurement operators and hence have no effect on the final state.

Note that $\eta_{e_0}(t) = -1$ marks the presence of Pauli error on the edge e_0 at time t and $\eta_{e_0}(t) = +1$ otherwise. The associated Pauli operator is $X_{\{\eta_{e_0}(t)\}} = \prod_{e_0} (\delta_{\eta_{e_0}(t), +1} I + \delta_{\eta_{e_0}(t), -1} X_{e_0})$.

3. Perform a round of syndrome measurement between each time interval $[t, t + 1]$. The syndrome measurements are also imperfect and their strength of measurement is set as β . Suppose the measurement outcome at time interval $[t, t + 1]$ is $\{s_{p_0}(t)\}$, then the associated action of imperfect measurement is $M_{\{s_{p_0}(t)\}}$.
4. After T rounds of syndrome measurements, we decode and apply Pauli X correction to the final state. We denote the correction operator as X_R .

Notice that with our definition of code space $\tilde{\mathcal{C}}$, the imperfection of syndrome measurement only affects syndrome bits but does not disturb logical information. We have known that any state in $\tilde{\mathcal{C}}$ takes the form as shown in Eq. (S17). Acting successive imperfect measurement operators on it still only affects the stabilizer bits. The logical information $|L\rangle$ will be left unchanged.

We might represent our error correction procedure as a diagram in Fig. 3(a). We will show that when the error chains of the whole history and the correction chain together constitute a contractible loop (correction operator and Pauli error operators forms stabilizer) the logical information is still preserved. Notice that the commutation between $M_{\{s_{p_0}(t)\}}$ and Pauli error $X_{\{\eta_{e_0}(t')\}}$ can be expressed as

$$M_{\{s_{p_0}(t)\}} X_{\{\eta_{e_0}(t')\}} = X_{\{\eta_{e_0}(t')\}} M_{\{s_{p_0}(t)\mu_{p_0}(t')\}}. \quad (\text{S18})$$

Here $\{\mu_{p_0}(t')\}$ represents the correct syndrome that should be generated by Pauli error $X_{\{\eta_{e_0}(t')\}}$. In other words, $\mu_{p_0}(t') = -1$ when p locates at the boundary of the error chain $\{\eta_{e_0}(t')\}$ and $\mu_{p_0}(t') = 1$ otherwise. The boundary configuration can also be represented by $\eta_{e_0}(t')$, that is $\mu_{p_0}(t') = \prod_{e_0 \in \partial p_0} \eta_{e_0}(t')$. Using this commutation relation we can move all Pauli error chains in Fig. 3(a) to the top and arrive at Fig. 3(b). When the operator $X_R X_{\{\eta_{e_0}(t)\}} \cdots X_{\{\eta_{e_0}(1)\}}$ forms a product of A_{v_0} operators, it will be commuting with imperfect measurement operators and logical Pauli operators, and hence acts trivially on the state below. Therefore we will obtain a final state as in Fig. 3(c). Though the final state is different from the original state $|\tilde{\Psi}\rangle$, it will be containing the same logical information, so we view this situation as a success of error correction.

Then we may compute the probability of syndrome outcomes given a particular error configuration $\{\eta_{e_0}(t)\}_t$

$$\begin{aligned} P(\{s_{p_0}(t)\}_t | \{\eta_{e_0}(t)\}_t) &= \left\| \prod_t M_{\{s_{p_0}(t)\}} X_{\{\eta_{e_0}(t)\}} |\tilde{\Psi}\rangle \right\|^2 \\ &= \left\| \prod_t M_{\{s_{p_0}(t)\} \prod_{k \leq t} \mu_{p_0}(k)} |\tilde{\Psi}\rangle \right\|^2 = \langle \tilde{\Psi} | \prod_t E_{\{s_{p_0}(t)\} \prod_{k \leq t} \mu_{p_0}(k)} |\tilde{\Psi}\rangle. \end{aligned} \quad (\text{S19})$$

Here $\|\cdot\|^2$ denotes the state norm and the subscript t in $\{s_{p_0}(t)\}_t$ and $\{\eta_{e_0}(t)\}_t$ remind us that they are the syndrome and Pauli error configurations of all the time steps. First, note that this expression is a well-defined joint probability for the $s_{p_0}(t)$ variables. $P(\{s_{p_0}(t)\}_t | \{\eta_{e_0}(t)\}_t)$ is always non-negative, and it is normalized a

$\sum_{\{s_{p_0}(t)\}_t} P(\{s_{p_0}(t)\}_t | \{\eta_{e_0}(t)\}_t) = 1$, which could be verified by applying the normalization of POVM operator $\sum_{\{s_{p_0}\}} E_{\{s_{p_0}\}} = I$ for each time slice. Besides, we can check that it is the true probability of syndrome measurement on the physical level. For example, imagine we are performing error correction in the real world. At the time t we ask what the syndrome measurement probability for the current step is. Eq. (S19) tells us that it should be the probability at the t' step conditioned on the configurations of previous steps

$$\begin{aligned} P(\{s_{p_0}(t')\} | \{s_{p_0}(t)\}_{t < t'}, \{\eta_{e_0}(t)\}_t) &= \frac{\sum_{\{s_{p_0}(t)\}_{t > t'}} P(\{s_{p_0}(t)\}_t | \{\eta_{e_0}(t)\}_t)}{\sum_{\{s_{p_0}(t)\}_{t \geq t'}} P(\{s_{p_0}(t)\}_t | \{\eta_{e_0}(t)\}_t)} = \frac{\|\prod_{t \leq t'} M_{\{s_{p_0}(t)\}} X_{\{\eta_{e_0}(t)\}} |\tilde{\Psi}\rangle\|^2}{\|\prod_{t < t'} M_{\{s_{p_0}(t)\}} X_{\{\eta_{e_0}(t)\}} |\tilde{\Psi}\rangle\|^2} \\ &= \frac{\text{tr}(E_{\{s_{p_0}(t')\}} \rho)}{\text{tr}(\rho)}, \quad \rho = \left(X_{\{\eta_{e_0}(t')\}} \prod_{t < t'} M_{\{s_{p_0}(t)\}} X_{\{\eta_{e_0}(t)\}} \right) |\tilde{\Psi}\rangle \langle \tilde{\Psi}| \left(X_{\{\eta_{e_0}(t')\}} \prod_{t < t'} M_{\{s_{p_0}(t)\}} X_{\{\eta_{e_0}(t)\}} \right)^\dagger. \end{aligned} \quad (\text{S20})$$

We arrive at the actual POVM probability at the current error correction step. Note that it also does not depend on the Pauli errors after time t' . Calculate the expression in Eq. (S19) explicitly, we have

$$\begin{aligned} P(\{s_{p_0}(t)\}_t | \{\eta_{e_0}(t)\}_t) &= \frac{1}{\mathcal{Z}_{\{+\}}} \sum_{\{\sigma_{e_0}\}} e^{\beta_0 \sum_{p_0} b_{p_0}} \prod_{p_0, t} \frac{\exp(\beta b_{p_0} s_{p_0}(t) \prod_{k \leq t} \mu_{p_0}(k))}{2 \cosh \beta} \\ &= \frac{1}{\mathcal{Z}_{\{+\}} (2 \cosh \beta)^{NT}} \sum_{\{\sigma_{e_0}\}} \exp \left[\sum_{p_0} b_{p_0} \left(\beta_0 + \beta \sum_t s_{p_0}(t) \prod_{k \leq t} \mu_{p_0}(k) \right) \right]. \end{aligned} \quad (\text{S21})$$

Here $\mathcal{Z}_{\{+\}} = 4^N (\cosh^N \beta_0 + \sinh^N \beta_0)$ is the partition function of 2-d \mathbb{Z}_2 lattice gauge theory. The σ_{e_0} 's have the same origin as Eq. (S2) through expansion under computational basis. Note that the above expression is independent of the choice of $|\tilde{\Psi}\rangle$ in code space. This can be shown by expanding $|\tilde{\Psi}\rangle$ under logical basis $|\tilde{\Psi}\rangle = \Psi_{++} |++\rangle + \Psi_{+-} |+-\rangle + \Psi_{-+} |-+\rangle + \Psi_{--} |--\rangle$ and using Elitzur's theorem. Since the POVM operators $E_{s_{p_0}(t)}$ at different times and different plaquettes are all complete and commute with each other, we may view the above probability as a joint probability of syndrome outcomes at different spacetime points, and it is conditioned on the error configuration. Notice that the syndromes at different times are correlated by the physical spin σ_{e_0} . That is because the imperfect measurement at each time step alters the instant quantum state, which affects the syndrome probability at the next time step. We can also construct a joint probability for both syndrome outcomes and error configuration. Noticing that the probability of a given error configuration is

$$P(\{\eta_{e_0}(t)\}_t) = \prod_{e_0, t} q^{\frac{1+\eta_{e_0}(t)}{2}} (1-q)^{\frac{1-\eta_{e_0}(t)}{2}} = \prod_{e_0, t} \frac{\exp(K \eta_{e_0}(t))}{2 \cosh K}, \quad (\text{S22})$$

we have

$$\begin{aligned} P(\{s_{p_0}(t)\}_t, \{\eta_{e_0}(t)\}_t) &= P(\{s_{p_0}(t)\}_t | \{\eta_{e_0}(t)\}_t) P(\{\eta_{e_0}(t)\}_t) \\ &= \frac{1}{\mathcal{Z}_{\{+\}}} \prod_{e_0, t} \frac{\exp(K \eta_{e_0}(t))}{2 \cosh K} \sum_{\{\sigma_{e_0}\}} e^{\beta_0 \sum_{p_0} b_{p_0}} \prod_{p, t} \frac{\exp(\beta b_{p_0} s_{p_0}(t) \prod_{k \leq t} \prod_{e_0 \in \partial p_0} \eta_{e_0}(k))}{2 \cosh \beta} \\ &= \frac{1}{\mathcal{Z}_{\{+\}} (2 \cosh \beta)^{NT} (2 \cosh K)^{2NT}} \sum_{\{\sigma_{e_0}\}} \exp \left[K \sum_{e_0, t} \eta_{e_0}(t) + \sum_{p_0} b_{p_0} \left(\beta_0 + \beta \sum_t s_{p_0}(t) \prod_{k \leq t} \prod_{e_0 \in \partial p_0} \eta_{e_0}(k) \right) \right]. \end{aligned} \quad (\text{S23})$$

Here $K = -\frac{1}{2} \ln \frac{q}{1-q}$.

Then we shall discuss in detail how could we decode with the syndrome outcomes $\{s_{p_0}(t)\}_t$. We mainly follow the method used in Ref. [5]. It is convenient to consider the situation that our logical information is stored forever. We extend the initial time $t = 1$ to $-\infty$ and the final time $t = T$ to $+\infty$, which means that the syndrome measurement procedure is performed forever without beginning or end. The error correction procedure is represented as a 3-dimensional lattice in Fig. S4. The vertical plaquettes represent physical qubits at different times and the horizontal plaquettes mark syndrome outcomes. The Pauli X errors are associated with vertical plaquettes (horizontal dashed lines), and the measurement errors are associated with horizontal plaquettes (vertical dashed lines). A given syndrome forms a chain in 3-d spacetime, and we denote the syndrome chain as c_S^* . Note that c_S^* is a set of spacetime plaquettes

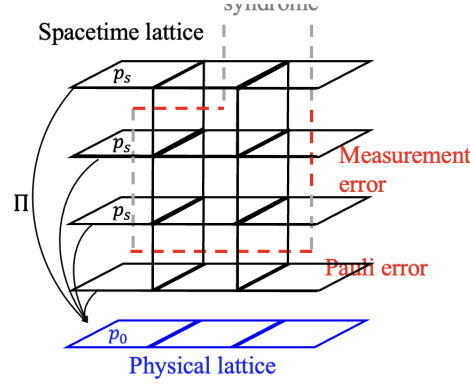


FIG. S4. 3-d spacetime of error history. The black lattice is the spacetime lattice, which takes periodic boundary condition in space directions and infinite boundary condition at time direction. The Pauli errors, measurement errors and error syndrome are represented as strings on the dual lattice (dashed lines). The horizontal red strings crossing timelike (vertical) plaquette represent the locations of Pauli X errors which actually act on the physical lattice (blue). The vertical gray strings crossing spacelike (horizontal) plaquettes represent the error syndrome, which marks the locations of measurement results $s_{p_0}(t) = -1$ at different time steps. The vertical red strings are where error syndromes do not match the Pauli errors that actually occurred which we view as measurement errors. Π denotes the projection from the 3-d spacetime lattice to the 2-d physical lattice.

and we view it as a chain on the dual lattice (dashed lines in Fig. S4). We can also view it as a \mathbb{Z}_2 valued vector with all the plaquettes as its basis. The task of the decoder is to find out both measurement errors and Pauli error with respect to the information of syndrome c_S^* . Denote the error chain of both measurement and Pauli errors as c_E^* , it obvious that c_E^* should have the same boundary as c_S^* , $\partial^* c_S^* = \partial^* c_E^*$. Here $\partial^* c_S^*$ is the set of cubics where the boundary points of c_S^* lie in. Suppose the error chain decided by the decoder is $c_{E'}^*$, when $c_{E'}^*$ and c_E^* are homologically equivalent, which means $c_{E'}^* + c_E^*$ forms contractible loop (here the plus is defined mod \mathbb{Z}_2), it should make no difference when we finally apply correction operator at $t = +\infty$, hence the error correction will be successful. But if $c_{E'}^* + c_E^*$ forms non-contractible loops, then the corresponding correction operator will be containing logical operator which has a nontrivial influence on logical information. In that case, the error correction will fail. So the task of the optimal decoder, named as maximum likelihood decoder, is to identify the equivalent class of error chain with the largest probability. Here the equivalent class of an error chain $[c_E^*]$ is defined as the set of all error chain that are homologically equivalent to c_E^* .

The probability of error chain class could be derived from Eq. (S23). Notice that measurement error configuration can be inferred from the syndrome at that moment and error configuration in the past

$$\eta_{p_0}(t) = s_{p_0}(t) \prod_{k \leq t} \mu_{p_0}(k) = s_{p_0}(t) \prod_{k \leq t} \prod_{e_0 \in \partial p_0} \eta_{e_0}(k). \quad (\text{S24})$$

Substitute the above equation into Eq. (S23), we obtain the joint probability of both measurement and Pauli error

$$P(\{\eta_{p_0}(t)\}_t, \{\eta_{e_0}(t)\}_t) = \frac{1}{\mathcal{Z}_{\{+\}} \prod_t [(2 \cosh \beta)^N (2 \cosh K)^{2N}]} \times \sum_{\{\sigma_{e_0}\}} \exp \left[K \sum_{e,t} \eta_{e_0}(t) + \sum_{p_0} b_{p_0} \left(\beta_0 + \beta \sum_t \eta_{p_0}(t) \right) \right]. \quad (\text{S25})$$

In this expression, we see that measurement errors at different time steps are correlated. Generally, the presence of measurement error increases the probability of measurement error at later times. We reinterpret the above equation on the 3-d lattice. Given an error chain in 3-d spacetime c_E^* , we still mark the location of error as $\eta_p = -1$. Specifically measurement error at a spacelike plaquette is denoted as $\eta_{p_s} = -1$. Pauli error at a timelike plaquette is denoted as

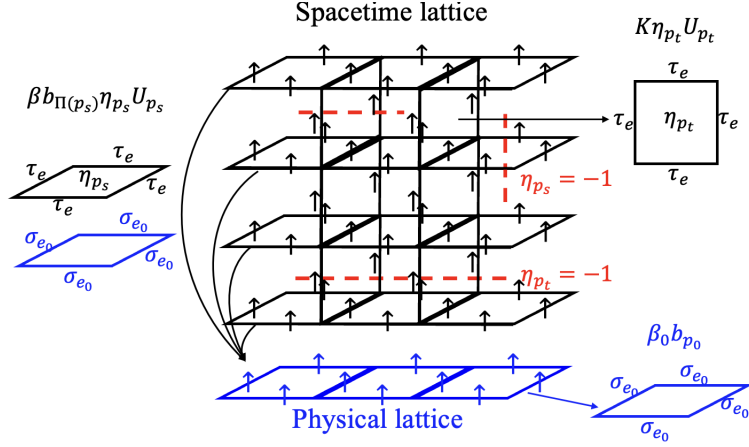


FIG. S5. Illustration of the SM model we obtained. The τ_e spins are defined on the edges of 3-d spacetime lattice and the σ_{e_0} . There are three types of interactions in this model. $\beta_0 b_{p_0}$ is the gauge interaction term defined on the physical lattice. $K\eta_{p_t}U_{p_t}$ is the timelike gauge interaction on spacetime lattice. The $\beta b_{\Pi(p_s)}\eta_{p_s}U_{p_s}$ term couples the spacelike gauge interaction term U_{p_s} to the gauge interaction term $b_{\Pi(p_s)}$ on physical lattice. The η_p 's set the signs of gauge interactions on the spacetime lattice.

$p_t = -1$. Then the probability of the error chain is expressed as

$$P(c_E^*) = P(\{\eta_p\}) = \frac{1}{\mathcal{Z}_{\{+\}} \prod_t [(2 \cosh \beta)^N (2 \cosh K)^{2N}]}$$

$$\times \sum_{\{\sigma_{e_0}\}} \exp \left[K \sum_{p_t} \eta_{p_t} + \beta_0 \sum_{p_0} b_{p_0} + \beta \sum_{p_s} b_{\Pi(p_s)} \eta_{p_s} \right]. \quad (\text{S26})$$

Note that σ_{e_0} 's and associated b_{p_0} 's are viewed as lying on a 2-d lattice distinct from the 3-d spacetime representing error correction history. Each p_s is associated with an $b_{\Pi(p_s)}$ on the 2-d physical lattice such that p_s and $\Pi(p_s)$ correspond to the same space point as in Fig. S4.

The probability of error class $[c_E]$ is calculated as a summation of probabilities of error chains that belong to the same equivalent class:

$$P([c_E]) = \sum_{c \in [c_E]} P(c) \quad (\text{S27})$$

This summation can be done by introducing virtual spin $\tau_p = \pm 1$ associated with each spacetime plaquette and relating it to each edge through \mathbb{Z}_2 gauge interaction [5], as in Fig. S5. The summation of homologically equivalent error chains yields the same result as the summation of configurations of virtual spins τ_e defined on edges up to factor counting the number of 1-form symmetry operations since the sign changing of τ_e corresponds to a deformation of error chain (see Fig. S6) and thus relates homologically equivalent error chains.:

$$P([c_E]) = \frac{1}{\mathcal{N}_1} \sum_{\{\tau_p\}} P(\{\eta_p \prod_{e \in \partial p} \tau_e\})$$

$$= \frac{1}{\mathcal{N}_1 \mathcal{Z}_{\{+\}} \prod_t [(2 \cosh \beta)^N (2 \cosh K)^{2N}]}$$

$$\times \sum_{\{\sigma_{e_0}\}, \{\tau_e\}} \exp \left[\beta_0 \sum_{p_0} b_{p_0} + \beta \sum_{p_s} \left(b_{\Pi(p_s)} \eta_{p_s} \prod_{e \in \partial p_s} \tau_e \right) + K \sum_{p_t} \left(\eta_{p_t} \prod_{e \in \partial p_t} \tau_e \right) \right]. \quad (\text{S28})$$

Here \mathcal{N}_1 denotes the number of 1-form symmetry operations and it diverges for infinite time T . We now arrive at a M model including both virtual spins $\{\tau_p\}$ on the 3-d spacetime lattice and physical spins $\{\sigma_{e_0}\}$ on a distinct 2-space lattice. The virtual spins in this SM model describe the fluctuation of error chains in the same class. The physical spins are coupled to virtual spins on time-like plaquettes at all times since the probability of measurement errors a

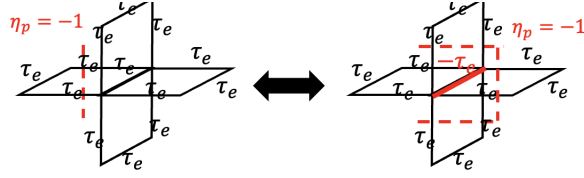


FIG. S6. Example of local symmetry. The red dashed lines represent the position where $\eta_p = -1$. The two $\{\eta_p\}$ configuration yield the same partition function by redefining the spin colored red. Pictorially, flipping τ_e spins is equivalent to a deformation of error chain.

certain time depends on the entire syndrome measurement history. The optimal decoding algorithm should select the error class $[c_E]$ with the largest $P([c_E])$. Moreover, if the interaction configuration $\{\eta_e\}$ is viewed as disordered with a correlated probability distribution $P(\{\eta_e\})$ defined in equation S26, then the deconfinement-confinement phase transition point of virtual spins $\{\tau_p\}$ in this disordered SM model should signify the error threshold of the error correction protocol as discussed in Ref. [5]. In summary, the quenched disordered SM model describing the error threshold is

$$\begin{aligned} \mathcal{Z}(\{\eta_p\}) &= \sum_{\{\sigma_{e_0}\}, \{\tau_e\}} \exp \left[\beta_0 \sum_{p_0} b_{p_0} + \beta \sum_{p_s} b_{\Pi(p_s)} \eta_{p_s} U_{p_s} + K \sum_{p_t} \eta_{p_t} U_{p_t} \right], \\ U_p &= \prod_{e \in \partial p} \tau_e, \quad b_{p_0} = \prod_{e_0 \in \partial p_0} \sigma_{e_0}, \\ P(\{\eta_e\}) &= \frac{\sum_{\{\sigma_{e_0}\}} \exp \left[\beta_0 \sum_{p_0} b_{p_0} + \beta \sum_{p_s} b_{\Pi(p_s)} \eta_{p_s} + K \sum_{p_t} \eta_{p_t} \right]}{\mathcal{Z}_{\{+\}} \prod_t [(2 \cosh \beta)^N (2 \cosh K)^{2N}]}. \end{aligned} \quad (\text{S29})$$

Note that in our SM model, all the spacelike plaquettes are coupled with the σ_{e_0} 's, causing a highly non-local correlation in the timelike direction. This is a consequence of the imperfect measurement in the initial state preparation. When the initial state is well prepared $\beta_0 \rightarrow +\infty$, all the b_{p_0} 's will be set to +1 in Eq. (S29) and we arrive at a random plaquette gauge model:

$$\begin{aligned} \mathcal{Z}(\{\eta_p\}) &= \sum_{\{\sigma_{e_0}\}, \{\tau_e\}} \exp \left[\beta \sum_{p_s} \eta_{p_s} U_{p_s} + K \sum_{p_t} \eta_{p_t} U_{p_t} \right], \\ U_p &= \prod_{e \in \partial p} \tau_e, \\ P(\{\eta_e\}) &= \frac{\exp \left[K \sum_{p_t} \eta_{p_t} + \beta \sum_{p_s} \eta_{p_s} \right]}{\prod_t [(2 \cosh \beta)^N (2 \cosh K)^{2N}]}, \end{aligned} \quad (\text{S30})$$

which is derived in Ref. [5] to describe the error threshold under probabilistic measurement error.

From Eq. (S29) we can sum the σ_e 's out and arrive at the SM model containing pure τ_e spins

$$\begin{aligned} \mathcal{Z}(\{\eta_p\}) &= \sum_{\{\tau_e\}} \left[\prod_{p_0} \cosh(\beta_0 + \beta \sum_t \eta_{p_s} U_{p_s}) + \prod_{p_0} \sin(\beta_0 + \beta \sum_t \eta_{p_s} U_{p_s}) \right] \exp \left[K \sum_{p_t} \eta_{p_t} \right], \\ P(\{\eta_e\}) &= \frac{1}{[(\cosh \beta_0)^N + (\sinh \beta_0)^N] \prod_t [(2 \cosh \beta)^N (2 \cosh K)^{2N}]} \\ &\times \left[\prod_{p_0} \cosh(\beta_0 + \beta \sum_t \eta_{p_s}) + \prod_{p_0} \sin(\beta_0 + \beta \sum_t \eta_{p_s}) \right] \exp \left[K \sum_{p_t} \eta_{p_t} \right]. \end{aligned} \quad (\text{S31})$$

III. LOCAL SYMMETRY ON NISHIMORI LINE

The SM model $\mathcal{Z}(\{\eta_p\})$ has a local symmetry when redefining the interaction background $\{\eta_p\}$

$$\eta_p \rightarrow \eta_p \prod_{e \in \partial p} \nu_e, \quad \tau_e \rightarrow \tau_e \nu_e, \quad \nu_e = \pm 1. \quad (\text{S32})$$

as in Fig. S6. More precisely, the partition function is invariant under redefinition of background interaction configuration $\{\eta_p\}$:

$$\mathcal{Z}(\{\eta_p \prod_{e \in \partial p} \nu_e\}) = \mathcal{Z}(\{\eta_p\}) \quad (\text{S33})$$

since the influence is absorbed in the summation of spin configuration by redefining spin variable $\tau'_e = \tau_e \nu_e$. Note that $\{\eta_p\}$ correspond to a representative error chain in error class $[c_E]$, and the local invariance Eq. (S32) tells us that $\mathcal{Z}(\{\eta_p\})$ does not depend on the choice of representative error chain. It only depends on the homological class of error chain.

We will use the local invariance S32 on Nishimori line to derive several results about the phase structure [6, 7]. Under the presence of disorder, to compute an expectation value, we should first take the ensemble average for a particular interaction configuration (denoted by $\langle \cdot \rangle_{\{\eta_p\}}$) and then take the disorder average on different configurations (denoted by $[\cdot]$). For a given observable $O(\{\eta_p\}, \{\sigma_{e_0}\}, \{\tau_e\})$ depending on the σ spins, τ spins and interaction configuration, these two kinds of averages are defined as:

$$\begin{aligned} \langle O \rangle_{\{\eta_p\}} &= \frac{1}{\mathcal{Z}(\{\eta_p\})} \sum_{\{\sigma_{e_0}\}, \{\tau_e\}} O \exp \left[\beta_0 \sum_{p_0} b_{p_0} + \beta \sum_{p_s} b_{\Pi(p_s)} \eta_{p_s} U_{p_s} + K \sum_{p_t} \eta_{p_t} U_{p_t} \right] \\ [\langle O \rangle_{\{\eta_p\}}] &= \sum_{\{\eta_p\}} P(\{\eta_p\}) \langle O \rangle_{\{\eta_p\}} \end{aligned} \quad (\text{S34})$$

If an observable $O(\{\eta_p\}, \{\sigma_{e_0}\}, \{\tau_e\})$ is also invariant under local symmetry transformation in Eq. (S32):

$$O(\{\eta_p \prod_{e \in \partial p} \nu_e\}, \{\sigma_{e_0}\}, \{\tau_e \nu_e\}) = O(\{\eta_p\}, \{\sigma_{e_0}\}, \{\tau_e\}) \quad (\text{S35})$$

then the expectation value can be evaluated as:

$$\begin{aligned} [\langle O \rangle] &= \sum_{\{\eta_p\}} \frac{P(\{\eta_p\})}{\mathcal{Z}(\{\eta_p\})} \sum_{\{\sigma_{e_0}\}, \{\tau_e\}} O(\{\eta_p\}, \{\sigma_{e_0}\}, \{\tau_e\}) \\ &\times \exp \left[\beta_0 \sum_{p_0} b_{p_0} + \beta \sum_{p_s} b_{\Pi(p_s)} \eta_{p_s} U_{p_s} + K \sum_{p_t} \eta_{p_t} U_{p_t} \right] \\ &= \sum_{\{\eta_p\}} \frac{P(\{\eta_p \prod_{e \in \partial p} \nu_e\})}{\mathcal{Z}(\{\eta_p \prod_{e \in \partial p} \nu_e\})} \sum_{\{\sigma_{e_0}\}, \{\tau_e\}} O(\{\eta_p \prod_{e \in \partial p} \nu_e\}, \{\sigma_{e_0}\}, \{\tau_e\}) \\ &\times \exp \left[\beta_0 \sum_{p_0} b_{p_0} + \beta \sum_{p_s} b_{\Pi(p_s)} \eta_{p_s} U_{p_s} \prod_{e \in \partial p_s} \nu_e + K \sum_{p_t} \eta_{p_t} U_{p_t} \prod_{e \in \partial p_t} \nu_e \right] \\ &= \sum_{\{\eta_p\}} \frac{P(\{\eta_p \prod_{e \in \partial p} \nu_e\})}{\mathcal{Z}(\{\eta_p\})} \sum_{\{\sigma_{e_0}\}, \{\tau_e\}} O(\{\eta_p\}, \{\sigma_{e_0}\}, \{\tau_e\}) \\ &\times \exp \left[\beta_0 \sum_{p_0} b_{p_0} + \beta \sum_{p_s} b_{\Pi(p_s)} \eta_{p_s} U_{p_s} + K \sum_{p_t} \eta_{p_t} U_{p_t} \right] \end{aligned} \quad (\text{S36})$$

$$\begin{aligned}
&= \frac{1}{2^{3NT}} \sum_{\{\nu_e\}} \sum_{\{\eta_p\}} \frac{1}{\mathcal{Z}(\{\eta_p\})} \sum_{\{\sigma_{e_0}\}, \{\tau_e\}} O(\{\eta_p\}, \{\sigma_{e_0}\}, \{\tau_e\}) \\
&\times \exp \left[\beta_0 \sum_{p_0} b_{p_0} + \beta \sum_{p_s} b_{\Pi(p_s)} \eta_{p_s} U_{p_s} + K \sum_{p_t} \eta_{p_t} U_{p_t} \right] \\
&= \frac{1}{2^{3NT} \mathcal{Z}_{\{+\}} (2 \cosh \beta)^{NT} (2 \cosh K)^{2NT}} \sum_{\{\sigma_{e_0}\}, \{\tau_e\}, \{\eta_p\}} O(\{\eta_p\}, \{\sigma_{e_0}\}, \{\tau_e\}) \\
&\times \exp \left[\beta_0 \sum_{p_0} b_{p_0} + \beta \sum_{p_s} b_{\Pi(p_s)} \eta_{p_s} U_{p_s} + K \sum_{p_t} \eta_{p_t} U_{p_t} \right]
\end{aligned}$$

In the third equality, we make use of the local symmetry. In the fourth equality we averaged over different $\{\nu_e\}$ since the final result $\langle O \rangle$ is independent of $\{\nu_e\}$. The fifth equality is obtained by noticing that:

$$\sum_{\{\nu_e\}} P(\{\eta_p\} \prod_{e \in \partial p} \nu_e) = \frac{\mathcal{Z}(\{\eta_p\})}{\mathcal{Z}_{\{+\}} (2 \cosh \beta)^{NT} (2 \cosh K)^{2NT}} \quad (\text{S37})$$

First we consider $O = W_{A_0} = \prod_{p_0 \in A_0} b_{p_0}$ which is the Wilson loop on 2-d physical lattice. Clearly, it satisfies Eq (S35). So we calculate its expectation value as:

$$\begin{aligned}
\langle W_{A_0} \rangle &= \frac{1}{2^{3NT} \mathcal{Z}_{\{+\}} (2 \cosh \beta)^{NT} (2 \cosh K)^{2NT}} \\
&\sum_{\{\sigma_{e_0}\}, \{\tau_e\}, \{\eta_p\}} W_{A_0} \exp \left[\beta_0 \sum_{p_0} b_{p_0} + \beta \sum_{p_s} b_{\Pi(p_s)} \eta_{p_s} U_{p_s} + K \sum_{p_t} \eta_{p_t} U_{p_t} \right] \\
&= \frac{1}{\mathcal{Z}_{\{+\}}} \sum_{\{\sigma_{e_0}\}} W_{A_0} \exp \left[\beta_0 \sum_{p_0} b_{p_0} \right] = \langle W_{A_0} \rangle_{\{+\}} \\
&= \frac{(\tanh \beta_0)^{|A_0|} + (\tanh \beta_0)^{N-|A_0|}}{1 + (\tanh \beta_0)^N}
\end{aligned} \quad (\text{S38})$$

Here $\langle \cdot \rangle_{\{+\}}$ denotes the expectation value for the pure 2-d \mathbb{Z}_2 gauge theory of physical spins σ_{e_0} , $\mathcal{Z}_{\{+\}} = \sum_{\{\sigma_{e_0}\}} \exp \left[\beta \sum_{p_0} b_{p_0} \right]$. Actually, the above derivation works for any observable contains purely σ_{e_0} spins. So we conclude that the σ_{e_0} spin in SM model shown in Eq. (S29) behaves exactly the same as pure 2-d \mathbb{Z}_2 gauge theory. Specifically for the Wilson loop W_{A_0} , we find it obeys area law for any finite β_0 , same as 2-d \mathbb{Z}_2 lattice gauge theory, so the σ_{e_0} spins always stays in disordered phase.

We may also compute the internal energy, which is also invariant under the transformation shown in Eq. (S32) given that

$$\begin{aligned}
\langle \eta_{p_s} b_{\pi(p_s)} U_{p_s} \rangle &= \frac{1}{2^{3NT} \mathcal{Z}_{\{+\}} (2 \cosh \beta)^{NT} (2 \cosh K)^{2NT}} \\
&\times \sum_{\{\sigma_{e_0}\}, \{\tau_e\}, \{\eta_p\}} \eta_{p_s} b_{\pi(p_s)} U_{p_s} \exp \left[\beta_0 \sum_{p_0} b_{p_0} + \beta \sum_{p_s} b_{\Pi(p_s)} \eta_{p_s} U_{p_s} + K \sum_{p_t} \eta_{p_t} U_{p_t} \right] \\
&= \frac{1}{2^{3NT} \mathcal{Z}_{\{+\}} (2 \cosh \beta)^{NT} (2 \cosh K)^{2NT}} \sum_{\{\sigma_{e_0}\}, \{\tau_e\}} (2 \sinh \beta) (2 \cosh \beta)^{NT-1} (2 \cosh K)^{2NT} \exp \left[\beta_0 \sum_{p_0} b_{p_0} \right] \\
&= \tanh \beta,
\end{aligned} \quad (\text{S39})$$

and similarly

$$\begin{aligned}
\langle \eta_{p_t} U_{p_t} \rangle &= \frac{1}{2^{3NT} \mathcal{Z}_{\{+\}} (2 \cosh \beta)^{NT} (2 \cosh K)^{2NT}} \\
&\times \sum_{\{\sigma_{e_0}\}, \{\tau_e\}, \{\eta_p\}} \eta_{p_t} U_{p_t} \exp \left[\beta \sum_{p_0} b_{p_0} + \beta \sum_{p_s} b_{\Pi(p_s)} \eta_{p_s} U_{p_s} + K \sum_{p_t} \eta_{p_t} U_{p_t} \right] \\
&= \frac{1}{2^{3NT} \mathcal{Z}_{\{+\}} (2 \cosh \beta)^{NT} (2 \cosh K)^{2NT}} \sum_{\{\sigma_{e_0}\}, \{\tau_e\}} (2 \sinh K) (2 \cosh \beta)^{NT} (2 \cosh K)^{2NT-1} \exp \left[\beta \sum_{p_0} b_{p_0} \right] \\
&= \tanh K,
\end{aligned} \tag{S40}$$

we have the expression for internal energy

$$\begin{aligned}
\mathcal{U} &= \left[-\beta \sum_{p_0} b_{p_0} - \beta \sum_{p_s} b_{\Pi(p_s)} \eta_{p_s} U_{p_s} - K \sum_{p_t} \eta_{p_t} U_{p_t} \right] \\
&= -N\beta \frac{\tanh \beta + (\tanh \beta)^{N-1}}{1 + (\tanh \beta)^N} - NT\beta \tanh \beta - 2NTK \tanh K.
\end{aligned} \tag{S41}$$

Then consider the Wilson loop for τ_e spins $W_A = \prod_{p \in A} U_p = \prod_{e \in \partial A} \tau_e$. Note that it is not invariant under Eq (S32). By a similar calculation as Eq. (S36) we have:

$$\begin{aligned}
\langle W_A \rangle &= \sum_{\{\eta_p\}} \frac{P(\{\eta_p\})}{\mathcal{Z}(\{\eta_p\})} \sum_{\{\sigma_{e_0}\}, \{\tau_e\}} W_A \exp \left[\beta \sum_{p_0} b_{p_0} + \beta \sum_{p_s} b_{\Pi(p_s)} \eta_{p_s} U_{p_s} + K \sum_{p_t} \eta_{p_t} U_{p_t} \right] \\
&= \sum_{\{\eta_p\}} \frac{P(\{\eta_p \prod_{e \in \partial p} \nu_e\})}{\mathcal{Z}(\{\eta_p\})} \sum_{\{\sigma_{e_0}\}, \{\tau_e\}} W_A \prod_{e \in \partial A} \nu_e \\
&\times \exp \left[\beta \sum_{p_0} b_{p_0} + \beta \sum_{p_s} b_{\Pi(p_s)} \eta_{p_s} U_{p_s} + K \sum_{p_t} \eta_{p_t} U_{p_t} \right] \\
&= \frac{1}{2^{3NT}} \sum_{\{\nu_e\}} \sum_{\{\eta_p\}} \frac{P(\{\eta_p \prod_{e \in \partial p} \nu_e\}) \prod_{e \in \partial A} \nu_e}{\mathcal{Z}(\{\eta_p\})} \sum_{\{\sigma_{e_0}\}, \{\tau_e\}} W_A \\
&\times \exp \left[\beta \sum_{p_0} b_{p_0} + \beta \sum_{p_s} b_{\Pi(p_s)} \eta_{p_s} U_{p_s} + K \sum_{p_t} \eta_{p_t} U_{p_t} \right] \\
&= \frac{1}{2^{3NT} \mathcal{Z}_{\{+\}} (2 \cosh \beta)^{NT} (2 \cosh K)^{2NT}} \sum_{\{\eta_p\}} \mathcal{Z}(\{\eta_p\}) \langle W_A \rangle^2 \\
&= \langle W_A \rangle^2
\end{aligned} \tag{S42}$$

The result $\langle W_A \rangle = \langle W_A \rangle^2$ signifies the absence of gauge glass phase ($\langle W_A \rangle = 0$, $\langle W_A \rangle^2 > 0$) on the Nishimori line [7].

In addition, one may find that the modified Wilson loop $W_A \prod_{p \in A} \eta_p$ is invariant under local symmetry. It can be

calculated as

$$\begin{aligned}
\langle [W_A \prod_{p \in A} \eta_p] \rangle &= \frac{1}{2^{3NT} \mathcal{Z}_{\{+\}} (2 \cosh \beta)^{NT} (2 \cosh K)^{2NT}} \\
&\times \sum_{\{\sigma_{e_0}\}, \{\tau_e\}, \{\eta_p\}} W_A \prod_{p \in A} \eta_p \exp \left[\beta_0 \sum_{p_0} b_{p_0} + \beta \sum_{p_s} b_{\Pi(p_s)} \eta_{p_s} U_{p_s} + K \sum_{p_t} \eta_{p_t} U_{p_t} \right] \\
&= \frac{1}{2^{3NT} \mathcal{Z}_{\{+\}} (2 \cosh \beta)^{NT} (2 \cosh K)^{2NT}} \sum_{\{\sigma_{e_0}\}, \{\tau_e\}} \exp \left[\beta_0 \sum_{p_0} b_{p_0} \right] \\
&\times \left(\prod_{p_s \in A_s} \sum_{\eta_{p_s}} \eta_{p_s} U_{p_s} \exp [\beta b_{\Pi(p_s)} \eta_{p_s} U_{p_s}] \prod_{p_s \notin A_s} \sum_{\eta_{p_s}} \exp [\beta b_{\Pi(p_s)} \eta_{p_s} U_{p_s}] \right) \\
&\times \left(\prod_{p_t \in A_t} \sum_{\eta_{p_t}} \eta_{p_t} U_{p_t} \exp [K \eta_{p_t} U_{p_t}] \prod_{p_t \notin A_t} \sum_{\eta_{p_t}} \exp [K \eta_{p_t} U_{p_t}] \right) \\
&= \frac{1}{2^{3NT} \mathcal{Z}_{\{+\}} (2 \cosh \beta)^{NT} (2 \cosh K)^{2NT}} \sum_{\{\sigma_{e_0}\}, \{\tau_e\}} \exp \left[\beta_0 \sum_{p_0} b_{p_0} \right] \\
&\times \left(\prod_{p_s \in A_s} b_{\pi(p_s)} \right) (2 \sinh \beta)^{|A_s|} (2 \cosh \beta)^{NT - |A_s|} (2 \sinh K)^{|A_t|} (2 \cosh K)^{2NT - |A_t|} \\
&\langle W_{\Pi(A)} \rangle_{\{+\}} (\tanh \beta)^{|A_s|} (\tanh K)^{|A_t|}
\end{aligned} \tag{S43}$$

Here A_s and A_t denote the sets of spacelike plaquettes and timelike plaquettes contained in A respectively. Π is the projection onto physical lattice, see Fig. S9. This expression reveals that τ_e 's and σ_e 's are correlated and their Wilson loops somehow depend on each other. However, the modified Wilson loop $W_A \prod_{p \in A} \eta_p$ cannot serve as the correct order parameter for the error threshold.

SIV. LOW TEMPERATURE EXPANSION

The ordered (deconfinement) phase is expected to exist at the exact zero temperature point (on the Nishimori line $\beta_0, \beta, K \rightarrow +\infty$). Near the zero temperature point, we may perform a low-temperature expansion for Wilson loops to show if the ordered phase still persists to some finite temperature. Assume $e^{-\beta_0}$, $e^{-\beta}$, e^{-K} are of the same order, we expand $\langle [W_A] \rangle$ up to the order $e^{-4\beta}$ following the method discussed in Ref. [3].

We first perform the expansion for the disorder probability $P(\{\eta_p\})$. Through the expression of $P(\{\eta_p\})$

$$P(\{\eta_e\}) = \frac{2^{N+1} \sum_{\{b_{p_0}\}} \frac{1 + \prod_{p_0} b_{p_0}}{2} \exp \left[\beta_0 \sum_{p_0} b_{p_0} + \beta \sum_{p_s} b_{\Pi(p_s)} \eta_{p_s} + K \sum_{p_t} \eta_{p_t} \right]}{\mathcal{Z}_{\{+\}} \prod_t [(2 \cosh \beta)^N (2 \cosh K)^{2N}]}. \tag{S44}$$

We notice that the zeroth order is contributed by the configuration that all b_{p_0} and η_p are equal to +1. The order $e^{-2\beta}$ is given by flipping one of the η_p s to -1. The order $e^{-4\beta}$ is given by flipping any two of the η_p s or flipping two of b_{p_0} s. Note that the parity of $\{b_{p_0}\}$ configuration must be even. Then we find that the numerator is expanded as

$$\begin{aligned}
&2^{N+1} E^{N\beta_0 + NT\beta + 2NTK} \left[\delta_{\{+\}} + e^{-2K} \sum_{p_t} \delta_{\{p_t\}} + e^{-2\beta} \sum_{p_s} \delta_{\{p_s\}} \right. \\
&\left. \left[+ e^{-4K} \sum_{(p_t, p'_t)} \delta_{\{p_t, p'_t\}} + e^{-4\beta} \sum_{(p_s, p'_s)} \delta_{\{p_s, p'_s\}} + e^{-2\beta - 2K} \sum_{(p_s, p_t)} \delta_{\{p_s, p_t\}} + e^{-4\beta_0} \sum_{(p_0, p'_0)} \delta_{\{\Pi^{-1}(p_0, p'_0)\}} \right] \right]. \tag{S45}
\end{aligned}$$

Here (p, p') denotes a pair of different plaquettes. For example (p_s, p'_s) denotes a pair of spacelike plaquettes and the summation $\sum_{(p_s, p'_s)}$ is taken on all such pairs. We have used a simplified notation for the Kronecker delta.

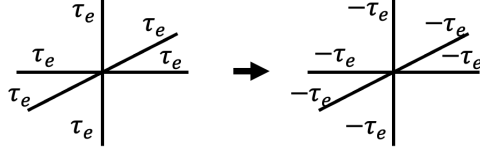


FIG. S7. Example of 1-form symmetry operation. The τ_e spins on a closed surface (surrounding the center vertex in this figure) are flipped.

symbol. δ_+ means that all the η_p s are fixed to be $+1$, $\delta_+ = \prod_p \delta_{\eta_p, +}$. δ_p denotes that η_p one the given plaquette is flipped to -1 , $\delta_p = \delta_{\eta_p, -} \prod_{p' \neq p} \delta_{\eta_{p'}, +}$, and similar for $\delta_{(p, p')}$, $\delta_{(p, p')} = \delta_{\eta_p, -} \delta_{\eta_{p'}, -} \prod_{p'' \neq p, p'} \delta_{\eta_{p''}, +}$. Finally, $\Pi^{-1}(p_0, p'_0)$ means that all the spacelike plaquettes whose projection on the physical lattice is p_0 or p'_0 are set to be -1 , $\delta_{\Pi^{-1}(p_0, p'_0)} = \prod_{p_s | \Pi(p_s) = p_0} \delta_{\eta_{p_s}, -} \prod_{p'_s | \Pi(p'_s) = p'_0} \delta_{\eta_{p'_s}, -} \prod_{p''_s | \Pi(p''_s) \neq p_0, p'_0} \delta_{\eta_{p''_s}, +}$. The number of integer times T should be sent to $+\infty$ at the end of the calculation. Combined with the denominator, we arrive at a perturbative expression for disorder probability

$$\begin{aligned}
P(\{\eta_p\}) &\simeq [1 - (1 - 2NTe^{-2K} - NTe^{-2\beta}) (2NTe^{-2K} + NTe^{-2\beta}) \\
&- \left(\binom{2NT}{2} e^{-4K} + \binom{NT}{2} e^{-4\beta} + 2(NT)^2 e^{-2K-2\beta} + \binom{N}{2} e^{-4\beta_0} \right)] \delta_{\{+\}} \\
&+ (1 - 2NTe^{-2K} - NTe^{-2\beta}) \left[e^{-2K} \sum_{p_t} \delta_{\{p_t\}} + e^{-2\beta} \sum_{p_s} \delta_{\{p_s\}} \right] \\
&+ e^{-4K} \sum_{(p_t, p'_t)} \delta_{\{(p_t, p'_t)\}} + e^{-4\beta} \sum_{(p_s, p'_s)} \delta_{\{(p_s, p'_s)\}} + e^{-2\beta-2K} \sum_{(p_s, p_t)} \delta_{\{(p_s, p_t)\}} + e^{-4\beta_0} \sum_{(p_0, p'_0)} \delta_{\{\Pi^{-1}(p_0, p'_0)\}}.
\end{aligned} \tag{S46}$$

Then we analyze the ensemble-averaged value for the interaction configurations that appeared in the above expression. Keeping in mind the fact that the interaction term U_p and Wilson loop W_A are both invariant under 1-form symmetry operations which flip the spins on a 2-d surface on the dual lattice as in Fig. S7, when performing the spin configuration summation for the lowest few orders we extract a factor of 1-form symmetry operation numbers \mathcal{N}_1 and evaluate the coefficient for each order on an equivalent class of spin configurations module 1-form symmetry.

First, consider the case all $\eta_p = +1$, and we want to compute

$$\langle W_A \rangle_{\{+\}} = \frac{1}{\mathcal{Z}(\{+\})} \sum_{\{\sigma_{e_0}\}, \{\tau_e\}} \left(\prod_{e \in \partial A} \tau_e \right) \exp \left[\beta_0 \sum_{p_0} b_{p_0} + \beta \sum_{p_s} b_{\Pi(p_s)} U_{p_s} + K \sum_{p_t} U_{p_t} \right]. \tag{S47}$$

The 0th order is contributed by the ground states, and a representative spin configuration is that all $\tau_e = +1$ and $p_0 = +1$. It leads to the term:

$$\mathcal{N}_1 2^{N+1} e^{N\beta_0 + NT\beta + 2NTK} \tag{S48}$$

in both the numerator and denominator. Now if we flip one of the τ_e spins to -1 , it increases the energy of four neighbor plaquettes and results in a term of order $e^{-8\beta}$, which is not included in our expansion. However, if we flip two b_{p_0} s, this only yields a term of order $e^{-4\beta_0}$ in the infinite boundary condition case. When two b_{p_0} s are flipped, it leads to -1 interactions on two strings of spacelike plaquettes corresponding to the position of b_{p_0} , as shown in S8 and it should cost infinite energy. However, the energy cost can be eliminated by the local symmetry transformation in Eq. (S32). The two strings can be viewed as merged together by setting the τ_e spins on the surface connecting them to -1 . Deformation of the surface is nothing but a 1-form symmetry operation and has already been mod out. Combining both the b_{p_0} configuration and the τ_e spin configuration, the total energy cost is just $4\beta_0$. Now consider the value of the Wilson loop. During the process of merging two strings together, if they cross the Wilson loop odd times, then exactly one of the spins on the boundary of region A will be flipped to -1 . So the value of the Wilson loop for that configuration is -1 . But if the Wilson loop is crossed for even times, it still gets $+1$. The total contribution of order $e^{-4\beta_0}$ is obtained by summing all the choices for flipping two b_{p_0} s, which contains $\binom{N}{2}$ terms

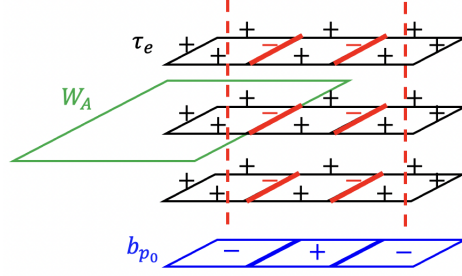


FIG. S8. Spin configuration when two b_{p_0} are flipped. The $\{b_{p_0}\}$ configuration is shown on the blue lattice. The timelike plaquettes are omitted for explicitness. The two red dashed strings represent the locations of -1 plaquette interaction cause by $b_{\Pi(p_s)} = -1$, and their energy cost can be eliminated by flipping the spins on the solid red edges.

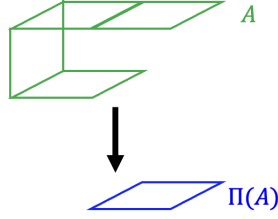


FIG. S9. The action of projection Π on surface A . The above surface lies inside 3-d spacetime and its projection on 2-d space is shown below. Their boundaries correspondingly are Wilson loops in 3-d spacetime and 2-d space.

By counting the number of odd time crosses, we obtain the expression for an additional term in the numerator

$$\left(\binom{N}{2} - 2|\Pi(A)|(N - |\Pi(A)|) \right) e^{-4\beta_0}. \quad (\text{S49})$$

Here we define $\Pi(A)$ as the projection of region A on the spacelike 2-d lattice module \mathbb{Z}_2 . The timelike plaquette are dropped under projection, and an even number of spacelike plaquettes on the same space position also leads to zero, as in Fig. S9. For denominator, the new term is just $\binom{N}{2} e^{-4\beta_0}$. So the expansion of $\langle W_A \rangle_{\{+\}}$ is evaluated as

$$\begin{aligned} \langle W_A \rangle_{\{+\}} &\simeq \frac{\mathcal{N}_1 2^{N+1} e^{N\beta_0 + NT\beta + 2NTK} \left[1 + \left(\binom{N}{2} - 2|\Pi(A)|(N - |\Pi(A)|) \right) e^{-4\beta_0} \right]}{\mathcal{N}_1 2^{N+1} e^{N\beta_0 + NT\beta + 2NTK} \left[1 + \binom{N}{2} e^{-4\beta_0} \right]} \\ &\simeq 1 - 2|\Pi(A)|(N - |\Pi(A)|) e^{-4\beta_0}. \end{aligned} \quad (\text{S50})$$

From this expression, we can roughly say that $\langle W_A \rangle_{\{+\}}$ decays with respect to the spacelike area.

Now we evaluated the Wilson loop configurations that only one η_p is flipped. Suppose a timelike plaquette p_t is flipped. Now the ground state energy is $2K$ higher than the previous all $\eta_p = +1$ case and the ground state spin configuration remains the same, which is all $\tau_e = +1$. The lowest excitation is caused by flipping one of the spins at the boundary of p_t , which has the extra energy $4K$. It eventually results in terms of order e^{-4K} . Notice that the probability of $\eta_{p_t} = -1$ is already of the order e^{-2K} , so we only need to concern about the ground state in our expansion, and it leads to

$$\langle W_A \rangle_{\{p_t\}} \simeq 1. \quad (\text{S51})$$

Similarly, for the spacelike plaquette flipping, we also have

$$\langle W_A \rangle_{\{p_s\}} \simeq 1. \quad (\text{S52})$$

Then we consider the configuration where two η_{p_s} are flipped. Notice that only the ground state contribution survives in our expansion since the probability is already of the order $e^{-4\beta}$. When the two flipped η_{p_s} do not contact each other, the representative spin configuration for ground state is still all $\tau_e = +1$ and only those two plaquette

where $\eta_p = -1$ have energy costs. But when the two flipped plaquettes are nearest neighbors, there will be two degenerate (ignoring the energetic difference between β and K) configurations that both have energy costs on two plaquettes. They are distinguished by whether the contacting edge of the two plaquettes is flipped to -1 . If the contacting edges lie on the Wilson loop, then summing the two degenerate configurations leads to $W_A = 0$. So assume the two flipped plaquettes are p and p' , then the Wilson loop takes the value

$$\langle W_A \rangle_{\{(p,p')\}} \simeq 1 - |\partial A \cap \partial p \cap \partial p'|. \quad (\text{S53})$$

If the two plaquettes and the Wilson loop intersect at one edge, $|\partial A \cap \partial p \cap \partial p'|$ takes 1. Otherwise, it takes 0. Consider the disorder summation of these configurations. Each edge connects to 4 plaquettes, yielding 6 pairs of nearest-neighbor plaquettes. By noticing that each timelike edge is associated with 6 pairs of timelike plaquettes while each spacelike edge is associated with a pair of timelike plaquettes, a pair of spacelike plaquettes and 4 combinations of spacelike and timelike plaquettes, we find that

$$\begin{aligned} e^{-4\beta} \sum_{(p_s, p'_s)} \langle W_A \rangle_{\{(p_s, p'_s)\}} &\simeq e^{-4\beta} \left(\binom{NT}{2} - |\partial A|_s \right) \\ e^{-4K} \sum_{(p_t, p'_t)} \langle W_A \rangle_{\{(p_t, p'_t)\}} &\simeq e^{-4K} \left(\binom{2NT}{2} - |\partial A|_s - 6|\partial A|_t \right) \\ e^{-2\beta-2K} \sum_{(p_t, p_s)} \langle W_A \rangle_{\{(p_t, p_s)\}} &\simeq e^{-2\beta-2K} (2(NT)^2 - 4|\partial A|_s). \end{aligned} \quad (\text{S54})$$

Here $|\partial A|_s$ denotes the number of spacelike edges in ∂A and $|\partial A|_t$ is the number of timelike edges in ∂A .

Finally we turn to the configuration denoted as $\{\Pi^{-1}(p_0, p'_0)\}$, which means all the spacelike interactions η_{p_s} along the timelike strings with the same space position as p_0 or p'_0 are flipped. In this case, a similar argument while evaluating Eq. (S50) could be applied. The two timelike strings are merged together by setting the spins in the interval to -1 , which gives us the ground state configuration. So the leading order of the Wilson loop is

$$\langle W_A \rangle_{\{\Pi^{-1}(p_0, p'_0)\}} \simeq \pm 1. \quad (\text{S55})$$

which takes -1 when only one of the p_0 and p'_0 stays in $\Pi(A)$ and takes $+1$ otherwise. Performing the disorder summation, we find that

$$e^{-4\beta_0} \sum_{(p_0, p'_0)} \langle W_A \rangle_{\{\Pi^{-1}(p_0, p'_0)\}} \simeq e^{-4\beta_0} \left(\binom{N}{2} - 2|\Pi(A)|(N - |\Pi(A)|) \right). \quad (\text{S56})$$

Putting all these stuff together, we arrive at the low-temperature expansion for the Wilson loop

$$\begin{aligned} [\langle W_A \rangle] &\simeq 1 - 4|\Pi(A)|(N - |\Pi(A)|)e^{-4\beta_0} - |\partial A|_s (e^{-4\beta} + e^{-4K} + 4e^{-2\beta-2K}) - 6|\partial A|_t e^{-4K} \\ &\simeq \exp \left[-4|\Pi(A)|(N - |\Pi(A)|)e^{-4\beta_0} - |\partial A|_s (e^{-4\beta} + e^{-4K} + 4e^{-2\beta-2K}) - 6|\partial A|_t e^{-4K} \right]. \end{aligned} \quad (\text{S57})$$

Note that the factor $|\Pi(A)|(N - |\Pi(A)|)$ appears because our space manifold is a closed surface. The result is naturally symmetric between $\Pi(A)$ and the 2-d complement of $\Pi(A)$. We also notice that the number of integer time t automatically vanishes in these expressions so they already suit the case $T \rightarrow +\infty$.

From Eq. (S57) we can see that once the initial state preparation suffers from imperfect measurement, the scaling behavior of Wilson loops becomes anisotropic for space and time direction. For a Wilson loop A purely containing spacelike plaquettes, we have

$$[\langle W_A \rangle] \simeq \exp \left[-4|A|(N - |A|)e^{-4\beta_0} - |\partial A| (e^{-4\beta} + e^{-4K} + 4e^{-2\beta-2K}) \right]. \quad (\text{S58})$$

For large enough N and large enough Wilson loop satisfying $|A| < N/2$, the area law decaying term dominates and the perimeter term can be ignored. So we conclude that the spacelike Wilson loop always decays with respect to the area at finite temperature even when the temperature is sufficiently low. Equivalently we can say that once the initial state is prepared under imperfect measurement, the spacelike Wilson loop always obeys area law. However, for a timelike Wilson loop, we will get:

$$[\langle W_A \rangle] \simeq \exp \left[- (e^{-4\beta} + e^{-4K} + 4e^{-2\beta-2K}) |\partial A|_s - 6e^{-4K} |\partial A|_t \right]. \quad (\text{S59})$$

o there will be a finite temperature phase for it to exhibit perimeter law scaling.

As we mentioned in the main text, the subtlety of Eq. (S57) is that we cannot directly take the thermodynamic limit $N \rightarrow \infty$. However, we may infer the thermodynamic result in analogy to the 2-d \mathbb{Z}_2 gauge theory. We may expand the Wilson loop for 2-d \mathbb{Z}_2 gauge theory Eq. (S38) also up to $e^{-4\beta_0}$:

$$\langle W_{A_0} \rangle_{\{+\}} \simeq 1 - 2|A_0|(N - |A_0|)e^{-4\beta_0}. \quad (\text{S60})$$

Compared with Eq. (S57) we find an approximate relation under low temperatures:

$$[\langle W_A \rangle] \simeq \langle W_{\Pi(A)} \rangle_{\{+\}}^2 \exp[-|\partial A|_s (e^{-4\beta} + e^{-4K} + 4e^{-2\beta-2K}) - 6|\partial A|_t e^{-4K}]. \quad (\text{S61})$$

In this expression $[\langle W_A \rangle]$ is a Wilson loop for τ_e spins and it relates to a Wilson loop $\langle W_{\Pi(A)} \rangle_{\{+\}}$ for σ_{e_0} spins on the 2-d physical lattice. Recall that $\langle \cdot \rangle_{\{+\}}$ denotes the expectation value for 2-d \mathbb{Z}_2 gauge theory $\mathcal{Z}_{\{+\}} = \int_{\{\sigma_{e_0}\}} \exp\left(\beta_0 \sum_{p_0} b_{p_0}\right)$. The expression in Eq. (S61) absorbs the size of space N and we expect it to valid under the thermodynamic limit. Turn back to Eq. (S38). If we take the $N \rightarrow +\infty$ limit first (keeping A_0 a finite region) and then perform low-temperature expansion, we arrive at

$$\langle W_{A_0} \rangle_{\{+\}} \simeq 1 - 2|A_0|e^{-2\beta_0} + 2|A_0|^2 e^{-4\beta_0}. \quad (\text{S62})$$

The difference between Eq. (S60) and Eq. (S62) arise from the criticality at zero temperature $\beta_0 = +\infty$. The $e^{-2\beta_0}$ term exhibit a discontinuity at zero temperature, which leads to the non-commuting of $N \rightarrow +\infty$ limit and $\beta_0 \rightarrow +\infty$ limit. A similar critical behavior should be found in $[\langle W_A \rangle]$. If the thermodynamic limit is taken before the low-temperature expansion, we infer that (not a rigorous proof)

$$[\langle W_A \rangle] \simeq \exp[-4|\Pi(A)|e^{-2\beta_0} + 4|\Pi(A)|^2 e^{-4\beta_0} - |\partial A|_s (e^{-4\beta} + e^{-4K} + 4e^{-2\beta-2K}) - 6|\partial A|_t e^{-4K}]. \quad (\text{S63})$$

In all, we expect that spacelike Wilson loops still decay with respect to area under the thermodynamic limit. Another way to think about the area law of spacelike Wilson loops when $N \rightarrow +\infty$ is to reconsider an open boundary condition at the spacelike directions and take an infinitely large system size before calculating the low-temperature expansion. Then an odd number of flipped b_{p_0} is allowed since we can send one in a pair of b_{p_0} 's to the infinity and eliminate it. Thus up to the leading order we have $[\langle W_A \rangle] \simeq \exp[-4|\Pi(A)|e^{-2\beta_0}]$. Although this open boundary condition does not correspond to any QEC procedure, we expect that the phase structure of the SM model does not depend on the choice of spacelike boundary conditions, and the expectation values of the order parameter for both the two kinds of boundary conditions should match under the thermodynamic limit.

In addition, Eq. S61 implies that the area law behavior of spacelike Wilson loops is controlled by the finite temperature disordered phase of the 2-d physical σ_{e_0} spins. Note that the area law behavior of the Wilson loop $\langle W_{A_0} \rangle_{\{+\}}$ is used in Ref. [1, 2] to argue the absence of long-range entanglement in the imperfect initial state. So in some sense, Eq. (S61) relates the inability of correcting measurement errors to the absence of long-range entanglement through σ_{e_0} spins.

SV. BEHAVIOR OF THE LOGICAL FIDELITY

As we have mentioned in the main text, the measurement errors are unidentifiable even at low temperatures, in the sense that the multi-round syndrome measurement protocol will not be better than a single-round one, i.e. $T = 1$ of 2D decoder. So one might ask how the QEC behaves when $T = 1$.

Suppose the QEC initial state is the imperfect logical 00 state $|\widetilde{\Psi}\rangle = (|00\rangle = (|++\rangle + |+-\rangle + |-+\rangle + |--\rangle))/2$, we estimate the impact of measurement errors on the logical fidelity, that is the fidelity between the final state and the initial state. Consider the scenario where the temperature is low and the system is of considerable size. In accordance with the preceding discourse, a Pauli error on a single physical qubit will be confounded with measurement error having the same syndrome by the decoder. Consequently, the Pauli error will remain uncorrected. If the uncorrected Pauli error intersects with a logical Pauli Z operator, it acts as a logical error on the logical information $|L\rangle$ (refer to Eq. (S17)), leading to a logical fidelity ~ 0 . But if the Pauli error locates elsewhere on the lattice, one may check the effects of the Pauli error and the measurement operator with the same syndrome complement each other and lead to a fidelity ~ 1 , since they both flip the same stabilizer bits in Eq. (S17) but do not affect the logical information $|L\rangle$. Average all error configurations, since the number of configurations that a Pauli error intersects with logical Z is proportional to $d = \sqrt{N}$, we anticipate that the logical fidelity behaves as $1 - \text{const} \times d$. The logical fidelity is

uppressed by a large distance, which is a signal that the QEC system is above the true threshold (measurement error threshold in our work). Here the constant depends on the physical error rates β_0 , β and K but does not depend on the distance d , and it should drop to 0 when the initial state is ideal, $\beta_0 \rightarrow +\infty$.

In contrast, we compare it with the $T = 1$ case of Ref. [5], the 2D decoder suffering from stochastic measurement errors. The decoder in this case also mixes up a Pauli error with probabilistic measurement errors, but their effects do not complement each other, since the probabilistic measurement error is just noise on the classical readouts and does not affect the quantum state. Consequently the logical fidelity scales as $1 - \text{const} \times d^2$, where the constant depends on the probability of Pauli and measurement errors. This logical fidelity is also above the threshold. Surprisingly, it is worse than the one of our model. However, the logical fidelity under stochastic errors can be improved by increasing T and arriving at an effective QEC when $T \gg d$ [5], which is not possible in our model.

One might argue that although the non-local measurement errors suppress logical fidelity, the correction of other local errors might lead to other terms that increase with d and compete with non-local measurement errors. However, the non-local measurement error suppression should be the leading order contribution in the low-temperature limit. Moreover, if the system lies above the blue crossover in the light red region in Fig. 5(b) of the main text, the effect of non-local measurement errors overweights other local errors. Thus we believe that the non-local measurement error suppression could outweigh other terms in that region. Nonetheless, these statements are not rigorous proofs and require further studies.

SVI. INDEPENDENT AND IDENTICAL DISTRIBUTED (IID) COHERENT DEVIATION

Here we discuss the case where the rotation angle in the imperfect measurement model is IID instead of fixed to a specific value. In experiments, the implementation of multi-qubit gates unavoidably suffers from over or under-rotation. In the simplified imperfect measurement model we used (Fig. 1 (c) in the main text), $t = \pi/4 + \delta t$ while δt is the coherent deviation and $\delta t = 0$ corresponds to perfect projective measurement. It is more physical to assume δt is independently Gaussian distributed, with zero mean value and small standard deviation σ . The effective imperfect measurement operator on each plaquette reads [1]

$$M_{s_p} \propto \frac{1}{\sqrt{2}} (\cos t + s_p B_p \sin t), \quad (\text{S64})$$

where $s_p = \pm 1$ is the outcome. Note that all discussion in our main text depends only on the POVM operator,

$$E_{s_p} = M_{s_p}^\dagger M_{s_p} = \frac{1}{2} (1 + s_p B_p \cos 2\delta t), \quad (\text{S65})$$

since it determines the outcome probability of measurement. Although δt is a random variable with zero mean value, we can see that $\cos 2\delta t$ is an even function, $\cos 2\delta t = \cos(-2\delta t)$, so the effective measurement strength will depend on the variance. As an approximation, we may average it over δt and find that

$$\overline{E_{s_p}} = \frac{1}{2} (1 + s_p B_p e^{-2\sigma^2}). \quad (\text{S66})$$

It is a projective measurement only when $\sigma = 0$. We may also cast it into the form

$$\overline{E_{s_p}} \propto e^{\beta s_p B_p}, \quad \beta = \text{arctanh} e^{-2\sigma^2}, \quad (\text{S67})$$

and it will lead to similar results as in the main text. Although more strictly speaking, we should treat δt as quenched disorder in the SM model, it will lead to a much harder calculation and we believe that it will not lead to a qualitative difference.

SVII. CODE STATE PREPARATION PROCEDURE TO STAY IN THE DECODABLE REGION FOR A FINITE CODE

In finite-size quantum code, a critical concern is the engineering of code states to ensure their retention within the decodable phase, as depicted in Fig. 5 (b) of the main text. A viable strategy to achieve this involves conducting multiple rounds of stabilizer measurements during the state preparation phase. The underlying assumption in our prior analysis was the immediate encoding of logical information into the code state following a single round of

Stabilizer measurement \ Stochastic error	none	X error	X and Z error
Imperfect	$T_{\text{pre}} = \omega(\log d)$	$T_{\text{pre}} = \omega(\log d)$	$T_{\text{pre}} \gg d$
Projective	$T_{\text{pre}} = O(1)$	$T_{\text{pre}} = O(1)$	$T_{\text{pre}} = O(1)$

TABLE S1. The overhead of $|\widetilde{++}\rangle$ state preparation under different circumstances. Notice that we consider only the rounds of measurements in state preparation T_{pre} here, to be distinguished with the rounds in an error correction cycle T . In principle projective measurement can prepare an arbitrary logical state if we chose the input state carefully, while imperfect measurements cannot directly prepare general states.

preparation, as described by Equation (S3). However, a more practical approach entails postponing the introduction of logical information until after several rounds of measurement and decoding. This method aims to enhance the resilience of the initial logical state, thereby increasing its robustness against potential errors.

In the specific context of quantum state preparation, our methodology initiates with the product $+$ states, targeting the establishment of the $|\widetilde{++}\rangle$ logical state. This process involves executing T_{pre} rounds of B_p POVM measurements. To simplify our model without loss of generality, we define the outcome of the first-round measurement as $\{s_p = -\}$, achieved by adjusting the sign of the stabilizers. During this procedure, stochastic Pauli X errors may occur. Subsequent to these measurements, a decoding step is conducted followed by the application of a recovery protocol which yields an imperfect $|\widetilde{++}\rangle$ logical state. The resulting state, denoted as $|\widetilde{++}\rangle$, is characterized by an imperfect parameter approximately equal to $\beta_0 T_{\text{pre}}$ on most plaquettes. This state is further subject to ancillary X logical errors represented as X_l , and open-ended Pauli X string errors, denoted as X_c . Upon completion of these preparation steps, logical information is encoded by applying logical operators. After completing these code state preparation, the logical information is safeguarded through further error correction cycles, with performance evaluated using our theory outlined in earlier sections.

Unlike the perfect preparation case, the imperfect POVMs actually change the quantum state, i.e. they change the weight of the superposition of the opposite syndromes. Luckily, the final Pauli X recovery flips most of the unwanted superposition where $B_p = -1$ has a higher weight than $B_p = +$. The remaining unflipped syndromes are caused by open-ended X_c string near the T_{pre} time boundary, which are of the order $O(p^{|c|} e^{-4\beta_0})$ when both the measurement and stochastic error rates are small, where $|c|$ is the length of the string. While our prior analysis indicated a constant probability of logical X error chains in this process, the specific state $|\widetilde{++}\rangle$ remains unaffected by the logical X operator. Consequently, this allows for the high-probability preparation of a stable $|\widetilde{++}\rangle$ state.

Provided that we prepared an initial state with imperfect parameter $\sim \beta_0 T_{\text{pre}}$, the robustness of the logical information is enhanced. The effectiveness of subsequent error correction cycles in safeguarding logical information is still described by Fig. 5 (b) of the main text with $\mathcal{T}_r = 1/\beta_0$ rescaled. To stay in the decodable region even when increasing code distance d , T_{pre} has to scale larger than $\log d$, $T_{\text{pre}} = \omega(\log d)$. However, one should keep in mind that the measurement preparation procedure only works for logical X eigenstates, while other code states should be obtained by logical operation afterward. If one tries to directly prepare other states, the constant residual logical error will damage the process. We also mention that our discussion above applies to starting from product $|0\rangle$ state and preparing with A_v measurement. In that case, we need to initialize a logical Z eigenstate first.

The complexity of toric code preparation is significantly increased due to imperfect measurement, in contrast to the ideal scenario involving perfect projective measurement. The protocol of multi-round syndrome measurements initially proposed by Dennis et al. [5] to address stochastic measurement errors, serves a distinct function in the context of imperfect state preparation. This arises from the fundamental differences in the underlying SM obtained by iTPGM in the work of Dennis et al. [5] and the SM model in our study, also refer to Tab. I of the main text. In the former scenario, the strategy leverages redundant syndrome data to decode and correct measurement errors, with the iTPGM exhibiting a finite error correction threshold that enables suppression of erroneous strings. Conversely, in our investigation, the SM model lacks a finite phase capable of error correction, rendering direct preparation of general logical states via imperfect measurements unfeasible. Nevertheless, preparing specific states in a finite size code, notably the logical X basis states, remains achievable through multi-round measurement processes. These processes are crucial for reducing the effective temperature ($\mathcal{T}_0 = 1/\beta_0$) of the model's two-dimensional component. Specifically, in the realm of imperfect measurements compounded by stochastic X errors, a preparation time $T_{\text{pre}} = \omega(\log d)$ is

ecessary to lower γ_0 , thereby attenuating the emergence of non-local timelike error strings in subsequent error correction cycles. Note that we should distinguish the difference between the preparation time T_{pre} and the error correction cycle duration T . In Ref. [5] $T \gg d$ is required for a perfect code state under stochastic measurements and Pauli errors while they have not discussed about state preparation. In our case T_{pre} takes at least $\omega(\log d)$, and we anticipate $T \gg d$ is still necessary for the subsequent error correction cycle to further mitigate spacelike non-contractible error strings effectively.

Beyond the imperfect stabilizer measurements for X errors, stochastic Pauli Z errors may also occur during the preparation of the $|\widetilde{++}\rangle$ state. Consequently, it becomes necessary to repeatedly measure A_v stabilizers, which may also be subject to coherent noise, and to decode in order to mitigate logical Z errors. Fortunately, the physical product state $|+\rangle^{\otimes n}$ serves as an eigenstate for A_v stabilizers, rendering it an optimal initial state for addressing both Pauli Z errors and A_v syndromes. By mapping the Z decoding to an RPGM, one can argue that the logical Z errors are suppressed at low error rates, so the $|\widetilde{++}\rangle$ state preparation still works, although in that case we have to set $T \gg d$ as we are effectively performing an error correction cycle on Z errors. The overhead of $|\widetilde{++}\rangle$ state preparation is summarized in Tab. S1. Also, the preparation of $|\widetilde{00}\rangle$ could be tackled similarly using the X - Z duality. We also underscore that the 3D protocol for preparing specific logical Pauli basis states may not be applicable to more realistic preparation circuits, as will be discussed in the subsequent section. In this context, the further investigation of code space preparation becomes critically important and urgent.

SVIII. IMPERFECT CODE STATE OF THE REALISTIC CIRCUIT MODEL

Here we discuss the initial code state assuming the realistic B_{p_0} measurement circuit in Fig. 1(b) of the main text with imperfect 2-qubit gates. On each plaquette p_0 , the measurement operator is expressed as Eq. (24) of the main text, i.e.

$$\begin{aligned}
M_+ &= \frac{1}{2} (1 + C_4 B_{p_0}) \left(1 + C_1 \sum_{i \in p_0} \sigma_i^z + C_2 \sum_{i < j \in p_0} \sigma_i^z \sigma_j^z + C_3 B_{p_0} \sum_{i \in p_0} \sigma_i^z \right). \\
C_4 &= e^{-i2t} \cos^4 \frac{t}{2} + e^{-i2t} \sin^4 \frac{t}{2} \\
C_1 &= -\frac{ie^{i2t} \sin \frac{t}{2} \cos^3 \frac{t}{2} + i \sin \frac{t}{2} \cos^7 \frac{t}{2} + i \sin^7 \frac{t}{2} \cos \frac{t}{2}}{(e^{i2t} + \cos^4 \frac{t}{2})^2 - \sin^8 \frac{t}{2}} \\
C_2 &= -\frac{\sin^2 \frac{t}{2} \cos^2 \frac{t}{2}}{e^{i2t} + \cos^4 \frac{t}{2} + \sin^4 \frac{t}{2}} \\
C_3 &= \frac{ie^{i2t} \sin^3 \frac{t}{2} \cos \frac{t}{2} + i \sin^3 \frac{t}{2} \cos^5 \frac{t}{2} + i \sin^5 \frac{t}{2} \cos^3 \frac{t}{2}}{(e^{i2t} + \cos^4 \frac{t}{2})^2 - \sin^8 \frac{t}{2}}
\end{aligned} \tag{S68}$$

Here we assumed all measurement results are $+$. It models the presence of coherent calibration error of two-qubit gates in a superconducting platform [?]. The imperfect initial state prepared by the above model is given by

$$\begin{aligned}
|\widetilde{++}\rangle &\propto \left(\prod_{p_0} M_+ \right) \otimes_{e_0} |+\rangle \\
&\propto \prod_{p_0} \left(1 + C_1 \sum_{i \in p_0} \sigma_i^z + C_2 \sum_{i < j \in p_0} \sigma_i^z \sigma_j^z + C_3 B_{p_0} \sum_{i \in p_0} \sigma_i^z \right) \\
&\times \left[\left(1 + C_4 \prod'_{p_0} B_{p_0} \right) \otimes'_{p_0} \sum_{b_{p_0} = \pm} (1 + C_4 b_{p_0}) |B_{p_0} = b_{p_0}\rangle \right] \left[\otimes'_{v_0} |A_{v_0} = +\rangle \right] \otimes |++\rangle,
\end{aligned} \tag{S69}$$

The third line shows that the B_{p_0} syndromes are superposed as in Eq. (S17), which was the key point that leads to the failure of decoding in the simplified model. The second line can be viewed as additional coherent Z errors acting on the already imperfect state. They mainly affect the state's A_{v_0} components. Expanding the product in the second line, the result is a summation of Pauli Z chains with different coefficients. For simplicity, we examine the effect of a single Pauli chain $\prod_{i \in c} \sigma_i^z$. Each Pauli chain c can be decomposed into $Z_l \prod_{p_0 \in A} B_{p_0} \prod_{i \in l} \prod_{i \in c_{\text{min}}} \sigma_i^z$ where c_{min}

the shortest chain that connecting the end points ∂c , $Z_l = I$, Z_{l_1} , Z_{l_2} , or $Z_{l_1}Z_{l_2}$ could be the identity or logical operator depending on the logical class of c , and A is a set of plaquettes. The $\prod_{i \in c_{min}} \sigma_i^z$ part flip the sign of A_{v_0} at the endpoints, $|A_{v_0} = +\rangle \rightarrow |A_{v_0} = -\rangle$, while B_{p_0} operator only changes the phase of B_{p_0} basis $|B_{p_0} = +\rangle \rightarrow |B_{p_0} = +\rangle$, $|B_{p_0} = -\rangle \rightarrow -|B_{p_0} = -\rangle$ and leaves the probability of defect unchanged.

$$\prod_{i \in c} \sigma_i^z \left[\left(1 + C_4 \prod_{p_0}' B_{p_0} \right) \otimes_{p_0}' \sum_{b_{p_0} = \pm} (1 + C_4 b_{p_0}) |B_{p_0} = b_{p_0}\rangle \right] \left[\otimes_{v_0}' |A_{v_0} = +\rangle \right] \otimes |++\rangle$$

$$\left[\left(1 + C_4 \prod_{p_0}' B_{p_0} \right) \otimes_{p_0 \notin A}' \sum_{b_{p_0} = \pm} (1 + C_4 b_{p_0}) |B_{p_0} = b_{p_0}\rangle \otimes_{p_0 \in A}' \sum_{b_{p_0} = \pm} b_{p_0} (1 + C_4 b_{p_0}) |B_{p_0} = b_{p_0}\rangle \right] \quad (S70)$$

$$\left[\otimes_{v_0 \notin \partial c}' |A_{v_0} = +\rangle \otimes_{v_0 \in \partial c}' |A_{v_0} = -\rangle \right] \otimes \bar{Z}_l |++\rangle$$

Summing over all Pauli Z chains c , the main difference from Eq. (S17) is that A_{v_0} syndromes also becomes imperfect superposition instead of being exactly $+$ (and additionally small coherent logical errors). Starting with such an imperfect code state leads to a worse QEC performance.

-
- 1] G.-Y. Zhu, N. Tantivasadakarn, A. Vishwanath, S. Trebst, and R. Verresen, Nishimori's cat: stable long-range entanglement from finite-depth unitaries and weak measurements (2022), [arXiv:2208.11136 \[quant-ph\]](#).
 - 2] J. Y. Lee, W. Ji, Z. Bi, and M. P. A. Fisher, Decoding measurement-prepared quantum phases and transitions: from Ising model to gauge theory, and beyond (2022), [arXiv:2208.11699 \[cond-mat.str-el\]](#).
 - 3] J. B. Kogut, An introduction to lattice gauge theory and spin systems, *Rev. Mod. Phys.* **51**, 659 (1979).
 - 4] S. Elitzur, Impossibility of spontaneously breaking local symmetries, *Phys. Rev. D* **12**, 3978 (1975).
 - 5] E. Dennis, A. Kitaev, A. Landahl, and J. Preskill, Topological quantum memory, *Journal of Mathematical Physics* **43**, 445 (2002).
 - 6] H. Nishimori, Internal Energy, Specific Heat and Correlation Function of the Bond-Random Ising Model, *Progress of Theoretical Physics* **66**, 1169 (1981).
 - 7] C. Wang, J. Harrington, and J. Preskill, Confinement-higgs transition in a disordered gauge theory and the accuracy threshold for quantum memory, *Annals of Physics* **303**, 31 (2003).